Series 11 Engineering Mechanisms 02

A Numerical Formulation for Moisture Migration in Masonry

G.P.A.G. van Zijl

Delft University Press

A Numerical Formulation for Moisture Migration in Masonry

Series 11: Engineering Mechanisms
02

A Numerical Formulation for Moisture Migration in Masonry

G.P.A.G. van Zijl

Delft University Press / 1999

Published and distributed by:

Delft University Press
P.O. Box 98
2600 MG Delft
The Netherlands
Telephone +31 (0)15 278 32 54
Fax +31 (0)15 278 16 61
e-mail: DUP@DUP.TUDelft.NL

by order of:

Faculty of Aerospace Engineering
Delft University of Technology
Kluyverweg 1
P.O. Box 5058
2600 GB Delft
The Netherlands
Telephone +31 (0)15 278 14 55
Fax +31 (0)15 278 18 22
e-mail: Secretariaat@LR.TUDelft.NL
website: http://www.lr.tudelft.nl

Cover: Aerospace Design Studio, 66.5 x 45.5 cm, by:
Fer Hakkaart, Dullenbakkersteeg 3, 2312 HP Leiden, The Netherlands
Tel. +31 (0)71 512 67 25

90-407-1893-8

Printed in The Netherlands

ACKNOWLEDGMENTS

The author wishes to express his gratitude towards Prof. René de Borst and Dr. Jan Rots for their support and guidance during the course of this work. The discussions with Dr. Leo Pel and Ir. Harold Brocken of Eindhoven University of Technology regarding their experience with measuring and knowledge of moisture migration in masonry were fruitful and contributed towards the chosen modelling approach. A word of thanks is directed towards Ir. Rob van der Pluijm and Ir. At Vermeltfoort, also of Eindhoven University of Technology, who are always willing to share and discuss their experimental results, enabling the essential verification and validation of the numerical models presented here.

The financial support by the Netherlands Technology Foundation (STW) under grant DCT-44.3406, as well as CUR-A33 is gratefully acknowledged.

The calculations were done on a computers of the Delft University of Technology, kept running smoothly by Harold Thung. The value of the stimulating working environment created by my room-mates, Harm Askes and Akke Suiker, is not to be under-estimated.

CONTENTS

1 INTRODUCTION 1

2 MATHEMATICAL DESCRIPTION 3

2.1 Non-linear diffusion theory . . . 3

2.2 Initial and boundary conditions . . . 5

2.3 Moisture migration in a two-phase medium . . . 5

2.4 Coupling with mechanical response . . . 6

3 NUMERICAL SOLUTION 7

3.1 Weighted residual formulation . . . 7

3.2 Finite Element formulation . . . 7

3.3 Time integration . . . 8

3.4 Incremental iterative solution procedure . . . 9

4 DETERMINATION OF THE MODEL PARAMETERS 11

4.1 Hygroscopic relation: $\theta - h$ . . . 11

4.2 Diffusivity coefficient . . . 12

5 SIMULATION OF MASONRY CREEP AND SHRINKAGE EXPERIMENTS 15

5.1 Modelling approach . . . 17

5.2 Model parameters: moisture migration . . . 17

5.3 Model parameters: mechanical behaviour . . . 18

5.4 Spatial and time discretisation . . . 22

5.5 Boundary conditions and initial values . . . 22

5.6 Results: Calcium silicate element (KZE) specimen . . . 24

5.7 Results: Calcium silicate brick (KZB) specimen . . . 28

5.7.1 Assumed moisture migration parameters . . . 28

5.7.2 KZB results for the assumed moisture migration parameters . . . 28

5.8 Mesh objectivity . . . 33

5.9 Sensitivity study . . . 35

5.9.1 Moisture content dependence on surface convection coefficient . . . 35

5.9.2 Shrinkage coefficient dependence on humidity 36
5.9.3 Pickett effect 37
5.9.4 Creep/relaxation 39
5.10 Discussion 39

6 EXPERIMENTAL PROGRAM: PROPOSAL 43
6.1 Moisture migration 44
6.1.1 Moisture diffusivity 44
6.1.2 Hygroscopic curves 46
6.1.3 Shrinkage coefficient 46
6.2 Parameters of mechanical behaviour 47
6.2.1 Specimen size and shape 47
6.2.2 Specimen types and fabrication 48
6.2.3 Experimental set-up and procedure 49
6.2.4 Measurements 49
6.2.5 Estimates of load levels and deformations 50
6.2.6 Exposure to avoid cracking ánd excessive drying time 51
6.3 Validation experiments on wall parts 58
6.3.1 Specimen size and shape 58
6.3.2 Specimen types and fabrication 59
6.3.3 Experimental set-up and procedure 59
6.3.4 Measurements 61
6.3.5 Estimates of load levels and deformations 62

7 CONCLUSION 65

A TWO-PHASE DIFFUSION: PERFECT HYDRAULIC INTERFACE 67

B COEFFICIENT SMOOTHNESS: TIME AND SPATIAL DISCRETISATION CONSTRAINT 69

C PLANE (2D) ANALYSIS VS. 3D ANALYSIS 73

D OVERSHOOT: TIME AND SPATIAL DISCRETISATION CONSTRAINT 75

REFERENCES 77

LIST OF FIGURES 79

LIST OF TABLES 81

Chapter 1

INTRODUCTION

The moisture content and moisture migration in cementitious materials determine their time dependent response, denoted by the terms creep and shrinkage. Much research has been done over the last decades to gain insight in these phenomena and to distinguish between true and apparent mechanisms of creep and shrinkage. However, both experimentally and computationally much remains to be done to characterise the true material shrinkage, stress-induced shrinkage, basic creep and the coupled effect of cracking and accelerated moisture migration. In this report and an accompanying report (Van Zijl 1999) these issues are addressed. Here a mathematical model and its finite element (FE) solution for analysing moisture migration, the underlying mechanism of shrinkage and creep in cementitious materials, are elaborated. In the accompanying report a model is described for the FE analysis of the mechanical response, namely creep, shrinkage and cracking.

As has become customary, the moisture migration is modelled as a diffusion-type process (eg. Bažant 1988, Pel 1995). It is expressed in terms of the pore humidity, as this quantity is directly linked to shrinkage and governs the conditions of convection at the boundary with air and continuous pressure across the interfaces with neighbouring cementitious materials.

It is assumed that the coupling with the mechanical response is weak, thus enabling solution of the diffusion equation in a separate/uncoupled manner from the the mechanical response. The hygral effects enter the latter process via the stress-free dimensional change and the viscosity of the deformational process, or bulk creep (Van Zijl 1999).

The material of interest is masonry, to be regarded as a particular cementitious concrete-like material. Experimental data obtained by Nuclear Magnetic Resonance (NMR) is employed to characterise the nonlinear diffusion coefficient (Pel 1995). Subsequently the model is employed in the analysis of creep and shrinkage of masonry specimen tested by Van der Pluijm and Wubs (1996). The dilemma of having measurements of only

the global response of masonry as a composite for estimating the model parameters is discussed comprehensively. This has inspired the proposal of an experimental program for the characterisation of all the model parameters required by the numerical model.

Chapter 2

MATHEMATICAL DESCRIPTION

The behaviour of cementitious materials depends strongly on their moisture content. It is therefore important to understand the moisture distribution in masonry, especially if the time-dependent phenomena of shrinkage and creep are to be analysed. In this chapter a mathematical formulation is elaborated for the modelling of the moisture migration in a porous medium.

2.1 Non-linear diffusion theory

The solution of the various moisture transport phenomena at the micro level in a porous medium, i.e. at the pore level, is hardly possible, due to the complexity of the pore geometry. Besides, for practical relevance a description at the macro level is required. However, the description of the phenomena at the micro level and subsequent volume averaging (Whitaker 1977, Bear and Bachmat 1990) facilitate setting up such a macroscopic formulation. In this spirit the Navier-Stokes equations for the microscopic *liquid* transport are volume-averaged, leading to Darcy's law for macroscopic liquid moisture flux

$$\boldsymbol{q_l} = -\boldsymbol{d}_{\theta l}\nabla\theta_l - \boldsymbol{d}_{Tl}\nabla T, \tag{2.1}$$

where θ_l is the volumetric liquid moisture content, T is the temperature, $\boldsymbol{d}_{\theta l}$ is the liquid moisture diffusivity and $\boldsymbol{d}_{Tl}$ is the thermal liquid moisture diffusivity. Fick's law for the *vapour* transport in the micro-pores is volume averaged, giving the expression for macroscopic vapour flux

$$\boldsymbol{q_v} = -\boldsymbol{d}_{\theta v}\nabla\theta_l - \boldsymbol{d}_{Tv}\nabla T, \tag{2.2}$$

where $\boldsymbol{d}_{\theta v}$ is the vapour moisture diffusivity and $\boldsymbol{d}_{Tv}$ is the thermal vapour moisture diffusivity. By addition the total moisture flux is

$$\boldsymbol{q} = -\boldsymbol{d}_{\theta}\,\boldsymbol{\nabla}\theta_l - \boldsymbol{d}_T\,\boldsymbol{\nabla}T \tag{2.3}$$

where

$$\begin{aligned} \boldsymbol{d}_\theta &= \boldsymbol{d}_{\theta l} + \boldsymbol{d}_{\theta v} \\ \boldsymbol{d}_T &= \boldsymbol{d}_{Tl} + \boldsymbol{d}_{Tv}. \end{aligned} \tag{2.4}$$

By combining the results with the macroscopic descriptions of mass conservation the moisture flow in a non-saturated, porous medium under hygral and thermal gradients can be described by the nonlinear diffusion-type equation

$$\begin{aligned} \frac{\mathrm{d}\theta}{\mathrm{d}t} + \boldsymbol{\nabla} \cdot \boldsymbol{q} + Q &= 0 \\ \boldsymbol{q} &= -\boldsymbol{d}_\theta \, \boldsymbol{\nabla}\theta - \boldsymbol{d}_T \, \boldsymbol{\nabla} T \end{aligned} \tag{2.5}$$

where θ is the total moisture content in liquid phase θ_l and vapour phase θ_v and Q is the rate of moisture loss due to hydration. Note that gravitational effects on the moisture transport have been neglected. See for example Philip and De Vries (1957), Pel (1995), or Brocken (1998) for comprehensive discussions and the derivation of eq. (2.5).

The nonlinearity is caused by especially the moisture diffusivity being strongly dependent on the moisture content.

Because shrinkage and creep depend directly on the pore pressure, it is convenient to write the diffusion process in terms of the relative pore humidity

$$h = p/p_s, \tag{2.6}$$

with p the macroscopical pore pressure and p_s the macroscopical pore pressure at saturation. Now eq. (2.5) becomes

$$\begin{aligned} \frac{\mathrm{d}h}{\mathrm{d}t} &= -c^{-1} \left(\boldsymbol{\nabla} \cdot \boldsymbol{q} + Q \right) - \frac{\partial h}{\partial T} \frac{\partial T}{\partial t} \\ \boldsymbol{q} &= -\boldsymbol{d}_h \boldsymbol{\nabla} h, \end{aligned} \tag{2.7}$$

where

$$\begin{aligned} c &= \frac{\partial \theta}{\partial h} \\ \boldsymbol{d}_h &= \boldsymbol{d}_\theta c + \boldsymbol{d}_T \frac{\partial T}{\partial h}. \end{aligned} \tag{2.8}$$

The parameters in eq. (2.7) can be interpreted physically. The gradient of the hygroscopic relation c reflects the ability to absorb or release water under unit change in h. Furthermore, $\boldsymbol{d}_h$ has been shown to represent permeability (Bažant and Najjar 1971). An added benefit of this formulation is that the influence of the continued hydration can usually be ignored (Bažant 1988). If, in addition, isothermal conditions are assumed, eq. (2.7) reduces to

$$\begin{aligned} \dot{h} &= -c^{-1} \boldsymbol{\nabla} \cdot \boldsymbol{q} \\ \boldsymbol{q} &= -\boldsymbol{d}_h \boldsymbol{\nabla} h \\ \boldsymbol{d}_h &= \boldsymbol{d}_\theta c. \end{aligned} \tag{2.9}$$

Note that the overhead dot notation has been introduced for the time derivative. Often the fact that the coefficient of absorption c is approximately constant is exploited, for example for concrete in the range $0.2 \leq h \leq 0.95$, simplifying eq. (2.9) to

$$\dot{h} = \nabla \cdot (\boldsymbol{d}_\theta \nabla h) \,. \tag{2.10}$$

In this report the general case of eq. (2.9) will be considered. It is only valid in the hygroscopic range, i.e. where $\frac{\partial \theta}{\partial h}$ is defined. Beyond this range of moisture contents moisture is accumulated in the large pores. It is a well accepted fact that the migration of the water in these macro-pores does not contribute to shrinkage.

2.2 Initial and boundary conditions

A further advantage of employing pore humidity as potential for the diffusion equation is that the boundary conditions can be easily identified:

$$\begin{array}{lll} \textit{essential}, & \text{i.e. prescribed humidity:} & h_B = h_E \\ \textit{natural}, & \text{i.e. prescribed boundary flux:} & \boldsymbol{q} \cdot \boldsymbol{n} = -q_B \\ \textit{convective}: & & \boldsymbol{q} \cdot \boldsymbol{n} = \beta (h - h_E) \end{array} \tag{2.11}$$

with $\boldsymbol{n}$ the unit vector pointing outward, normal to the boundary, the subscript B denoting the boundary and the subscript E denoting the prescribed, or environmental value. The surface convection coefficient β, sometimes referred to as the film coefficient, is given by

$$\beta = \frac{\beta^* \, p_s}{\rho_l} \tag{2.12}$$

with β^* (s/m) the transfer coefficient depending mainly on air velocity and surface smoothness (Tammes and Vos 1984) and ρ_l (kg/m^3) the liquid moisture mass density.

2.3 Moisture migration in a two-phase medium

Masonry is a composite material comprising of bricks/blocks and mortar/lime. It is often assumed that brick/mortar interfaces are hydraulically perfect, i.e. the contact is perfect. This implies that the pressure, of which pore humidity is a measure, is considered to be continuous across the interface:

$$h_b = h_m. \tag{2.13}$$

where the subscript b denotes brick/block and the subscript m denotes mortar. However, recent studies of moisture transport across such brick/mortar interfaces have indicated

that the contact between the two masonry constituents may not be perfect (Pel 1995), calling for an interfacial hygral resistance to be included in the model (Brocken and Pel 1997). The same authors have since reported that by just slightly varying numerical modelling parameters, the assumption of perfect hydraulic contact does in fact enable numerical simulation of moisture transport across such interfaces (Brocken et al. 1997).

In the current study perfect contact is assumed, implying that, for the general case that the hygroscopic relations for brick and mortar differ, a discontinuity in moisture content occurs at the interface:

$$\theta_b(h_b) \neq \theta_m(h_m). \tag{2.14}$$

For a solution of the differential equation in terms of moisture content (2.5), this discontinuity would require the nonlinear constraint of the interfacial values, complicating the numerical modelling. This is another advantage of adopting the diffusion formalism in terms of the pore humidity (2.9). An example of a moisture migration analysis in masonry is given in Appendix A to illustrate the discontinuity at the interfaces between the phases.

2.4 Coupling with mechanical response

The mathematical formulation of the mechanical behaviour and its numerical solution is described in an accompanying report (Van Zijl 1999). There, the influence of the moisture migration on the mechanical response is elaborated in detail, rendering brief comments here on the treatment of the coupled problem sufficient.

Contradicting evidence about the coupling between stress-strain behaviour and moisture migration exists. L'Hermite and Mamillan (1968) concluded from water loss measurements of loaded and unloaded specimens that the drying rate is not stress dependent. On the other hand Tanabe and Ishikawa (1993) report a weight loss of between 0.1% and 0.3% due to the drainage of unhydrated water by compressive loading. This insignificant effect is ignored here, enabling a one-way coupling approach to be followed, where no mechanical influence enters the moisture diffusion formulation. The moisture migration influence is, however, included in the description of the mechanical behaviour (Van Zijl 1999).

Note that in the presence of wide cracks an increased drying rate is to be expected. This has been shown experimentally by comparing the drying rates of cracked and uncracked concrete specimens (Bažant et al. 1987). For the case of shrinkage induced cracking investigated in this report, wide cracks are not encountered. When, in addition to the self/*eigen*stressing caused by the hygral gradients, an external restraint to hygral dimensional change exists, as in the case study in the accompanying report, wide cracks may occur. However, this requirement for coupling between the mechanical and hygral response is ignored in this study for sake of simplicity.

Chapter 3

NUMERICAL SOLUTION

3.1 Weighted residual formulation

The diffusion equation (2.9) states the process at hand in the *strong* form, i.e. the conditions must be met at each material point. For numerical approximation the *weak* form is adopted. Now the conditions are met only in an average sense

$$\int_V W \left(c\dot{h} + \boldsymbol{\nabla} \cdot \boldsymbol{q} \right) \, \mathrm{d}V = \int_V W \epsilon \, \mathrm{d}V = 0, \tag{3.1}$$

where W is a weight function to force the error or residual ϵ to zero in a volume-averaged sense. To reduce the order of the differential equation and to introduce non-essential boundary conditions, the theorem of *Gauß* is applied, giving

$$\int_V W c\dot{h} \, \mathrm{d}V - \int_V \boldsymbol{\nabla} W \cdot \boldsymbol{q} \, \mathrm{d}V + \int_B W \boldsymbol{q} \cdot \boldsymbol{n} \, \mathrm{d}B = 0. \tag{3.2}$$

Assuming natural conditions at a part of the boundary B_N and surface convection on another part of the boundary B_C cf. eqs. (2.11,2.12), eq. (3.2) becomes

$$\int_V W c\dot{h} \, \mathrm{d}V - \int_V \boldsymbol{\nabla} W \cdot \boldsymbol{q} \, \mathrm{d}V + \int_{B_C} W \beta h \, \mathrm{d}B = \int_{B_N} W q_B \, \mathrm{d}B + \int_{B_C} W \beta h_E \, \mathrm{d}B. \tag{3.3}$$

3.2 Finite Element formulation

In the FE approach to solve eq. (3.3) the domain is discretised into finite elements. In stead of selecting trial functions that satisfy global boundary conditions, approximation or interpolation functions are selected to satisfy the element boundary conditions. A variable is approximated within each element as follows:

$$h^e = \boldsymbol{N}^e \boldsymbol{h}^e \tag{3.4}$$

where $\boldsymbol{N}_e$ is a matrix of element interpolation functions and $\boldsymbol{h}^e$ the vector of humidities at discrete points on the boundary and/or within the element. Also, in the Galerkin approach, the weight function W is chosen to be of the same class as the interpolation functions $\boldsymbol{N}$. By substitution of (3.4) and (2.9b), eq. (3.3) now becomes

$$\int_{V^e} \boldsymbol{N}^T c \boldsymbol{N} \dot{\boldsymbol{h}} \, \mathrm{d}V + \int_{V^e} (\boldsymbol{\nabla N})^T \boldsymbol{d}_h \boldsymbol{\nabla N} \boldsymbol{h} \, \mathrm{d}V + \int_{B_C^e} \boldsymbol{N}^T \beta \boldsymbol{N} \boldsymbol{h} \, \mathrm{d}B = \int_{B_N^e} \boldsymbol{N}^T q_B \, \mathrm{d}B + \int_{B_C^e} \boldsymbol{N}^T \beta h_E \, \mathrm{d}B \tag{3.5}$$

in each element. For clarity the superscripts e have been retained only on the symbols for the integration domains. Eq. (3.5) can be written symbolically as

$$\boldsymbol{C}^e \dot{\boldsymbol{h}}^e + \boldsymbol{D}_h^e \boldsymbol{h}^e = \boldsymbol{Q}^e \tag{3.6}$$

with

$$\begin{aligned} \boldsymbol{C}^e &= \int_{V^e} \boldsymbol{N}^T c \boldsymbol{N} \, \mathrm{d}V \\ \boldsymbol{D}_h^e &= \int_{V^e} (\boldsymbol{\nabla N})^T \boldsymbol{d}_h \boldsymbol{\nabla N} \, \mathrm{d}V + \int_{B_C^e} \boldsymbol{N}^T \beta \boldsymbol{N} \, \mathrm{d}B \\ \boldsymbol{Q}^e &= \int_{B_N^e} \boldsymbol{N}^T q_B \, \mathrm{d}B + \int_{B_C^e} \boldsymbol{N}^T \beta h_E \, \mathrm{d}B. \end{aligned} \tag{3.7}$$

By accumulation of contributions from all elements the system set of differential equations are assembled as

$$\boldsymbol{C} \dot{\boldsymbol{h}} + \boldsymbol{D}_h \boldsymbol{h} = \boldsymbol{Q}. \tag{3.8}$$

where $\boldsymbol{h}$ now contains the pore humidities at all the discrete points employed for discretising the domain.

3.3 Time integration

Eq. (3.8) is solved step-wise by direct time integration for each time step Δt at time $t + \alpha \Delta t$, $0 \leq \alpha \leq 1$ in a generalised trapezoidal fashion. Hereby the set of differential equations is converted to a set of ordinary equations

$$\boldsymbol{D}_h^* \boldsymbol{h}^* = \boldsymbol{Q}^* \tag{3.9}$$

with

$$\begin{aligned} \boldsymbol{h}^* &= {}^{t+\alpha\Delta t}\boldsymbol{h} \\ \boldsymbol{D}_h^* &= {}^{t+\alpha\Delta t}\boldsymbol{C} + \alpha \, \Delta t \; {}^{t+\alpha\Delta t}\boldsymbol{D}_h \\ \boldsymbol{Q}^* &= \alpha \, \Delta t \; {}^{t+\alpha\Delta t}\boldsymbol{Q} + {}^{t+\alpha\Delta t}\boldsymbol{C} \; {}^{t}\boldsymbol{h}. \end{aligned} \tag{3.10}$$

In eq. (3.10) use is made of the time derivative

$${}^{t+\alpha\Delta t}\dot{\boldsymbol{h}} = \frac{{}^{t+\alpha\Delta t}\boldsymbol{h} - {}^{t}\boldsymbol{h}}{\alpha \, \Delta t}. \tag{3.11}$$

In this study fully implicit *Euler backward* integration is used by selecting $\alpha = 1$.

3.4 Incremental iterative solution procedure

Due to the nonlinearity of eq. (3.9), caused by the dependence of the diffusivity and the moisture capacity on the pore humidity, an incremental-iterative solution procedure is followed:

$$\boldsymbol{h}^*_{i+1} = \boldsymbol{h}^*_i + (\boldsymbol{D}_{inc})^{-1} \left(\boldsymbol{Q}^*_i - \boldsymbol{D}^*_{h,i}\, \boldsymbol{h}^*_i \right), \tag{3.12}$$

where i denotes the convergence iteration number. Here, either the *regular* Newton-Raphson method is employed, rendering

$$\boldsymbol{D}_{inc} = \boldsymbol{D}^*_{h,i}, \tag{3.13}$$

or the modified Newton-Raphson method, when

$$\boldsymbol{D}_{inc} = \boldsymbol{D}^*_{h,1}. \tag{3.14}$$

Chapter 4

DETERMINATION OF THE MODEL PARAMETERS

4.1 Hygroscopic relation: $\theta - h$

The moisture capacity is derived from the *sorption* isotherm, or hygroscopic relation, as its gradient ($c(h) = \partial\theta/\partial h$). Because of the well known hysteretic behaviour for drying and wetting cycles the *desorption* isotherm is employed for the drying studied here. For concrete the most widely used sorption isotherm is the BET model (Brunauer et al. 1938) and more lately the BSB model (Brunauer et al. 1939). However, in this study desorption isotherms for masonry determined experimentally at Eindhoven University of Technology, are employed - Figure 4.1.

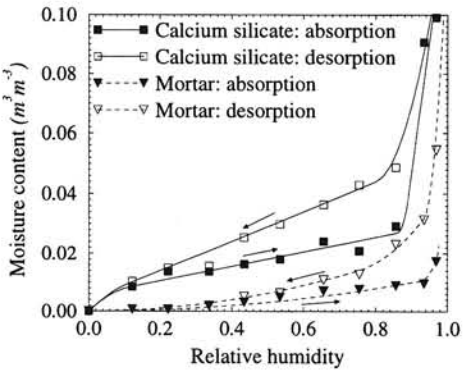

Figure 4.1: Isothermal sorption curves (Pel 1995) for masonry constituents.

4.2 Diffusivity coefficient

Due to the wide range in pore sizes in concrete the determination of the permeability $\boldsymbol{d}_h(h)$ or, alternatively, the moisture diffusivity $\boldsymbol{d}_\theta(h)$, eq. (2.9), is difficult. Indirect methods have been employed to fit test data (Bažant and Najjar 1971, Xi et al. 1993, Alvaredo 1994), as well as empirical formulas. Lately, the accurate measurement of moisture profiles has become possible with *Nuclear Magnetic Resonance* (NMR) (Pel 1995). A one-dimensional drying test setup and the NMR-measured moisture profiles are shown in Figure 4.2.

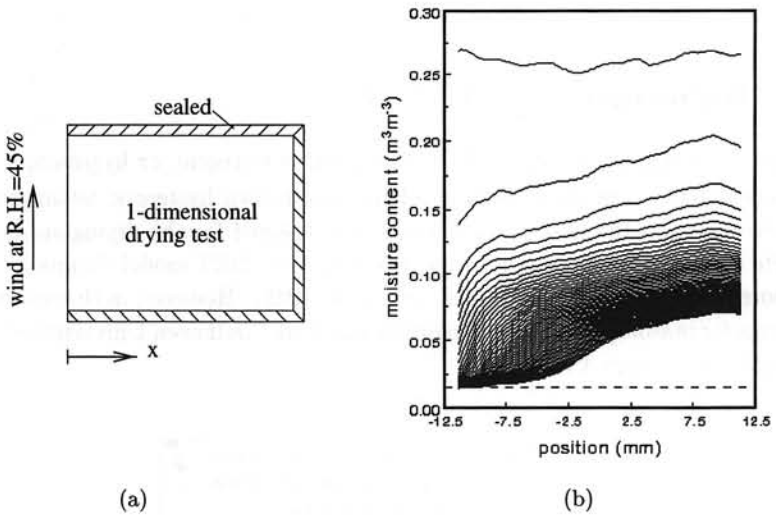

(a) (b)

Figure 4.2: (a) 1-Dimensional drying test for measuring (b) moisture profiles (Pel 1995), using NMR.

From these profiles the diffusivity coefficient can be derived by integration of eq. (2.5) for the one-dimensional, isothermal case with Q=0, yielding:

$$d_\theta = \frac{\int_L^{x'} \frac{\partial \theta}{\partial t} dx}{\left(\frac{\partial \theta}{\partial x}\right)_{x'}}. \tag{4.1}$$

In the above derivation use has been made of the zero flux boundary condition at the sealed end ($x = L$). A detailed description of the calculation of the nonlinear diffusivity from measured moisture profiles is given by Pel (1995). He also outlines the receding drying front method for characterisation of the diffusivity in the low moisture content

range. With the diffusivity coefficient determined in this manner, Figure 4.3, the moisture profiles can be reproduced numerically. This can be seen by comparing the numerically obtained moisture profiles, Figure 4.4, with the measured profiles, Figure 4.2b. Figure 4.4 shows the solutions of the governing equations in terms of (a) moisture content (2.5) and (b) pore humidity (2.9). In the latter case the pore humidity profiles are translated to moisture content via the hygroscopic relation. Note that care must be taken with regard to the smoothness of the parameter functions, as more strict time and spatial discretisation requirements exist for non-smooth parameters when solving for pore humidity from eq. (2.9). This matter is discussed in detail in Appendix B.

Pel (1995) ascribes the minimum and subsequent increasing diffusivity with moisture content decrease to the transition from liquid to vapour dominated moisture transport. However, a monotonically increasing diffusivity with increasing moisture content is found for the absorption, or wetting case, Figure 4.3. To investigate this phenomenon further, we consider the Boltzmann transformation, which reads for the one-dimensional case

$$\Gamma = \frac{x}{\sqrt{t}} \tag{4.2}$$

and by which the partial differential equation

$$\frac{\partial \theta}{\partial t} = \frac{\partial}{\partial x}\left(D_\theta \frac{\partial \theta}{\partial x}\right) \tag{4.3}$$

is transformed to the ordinary differential equation

$$\Gamma \frac{\mathrm{d}\theta}{\mathrm{d}\Gamma} + 2\frac{\mathrm{d}}{\mathrm{d}\Gamma}\left(D_\theta \frac{\mathrm{d}\theta}{\mathrm{d}\Gamma}\right) = 0 \tag{4.4}$$

if the diffusivity is spatially independent. By scaling all wetting moisture profiles with $1/\sqrt{t}$ they should coincide on a single $\theta - \Gamma$ relation, the solution of eq. (4.4). This is the case for the wetting of the building materials tested by Pel (1995), proving the spatial independence of the wetting diffusivity coefficient. For drying, however, this is not the case, indicating something like the so-called wall-effect in concrete (Alvaredo 1994), where the larger porosity of the upper/outer skin due to the casting process causes a higher diffusion rate than deeper in the concrete. Such a structural effect may, off course, not be included in a model parameter to be applied in the prediction of the response of specimens of other dimensions and subjected to other conditions. Thus some uncertainty prevails about the mechanism causing the increased diffusion at low moisture contents and thus the validity of the coefficient for drying. Nevertheless, it is accepted for the analyses in this report, as the low moisture content region of uncertainty is barely entered.

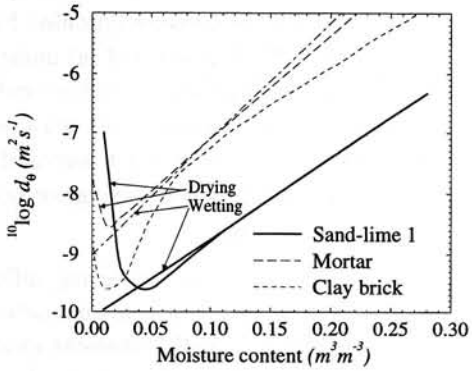

Figure 4.3: Diffusivity variation with moisture content for various building materials (Pel 1995).

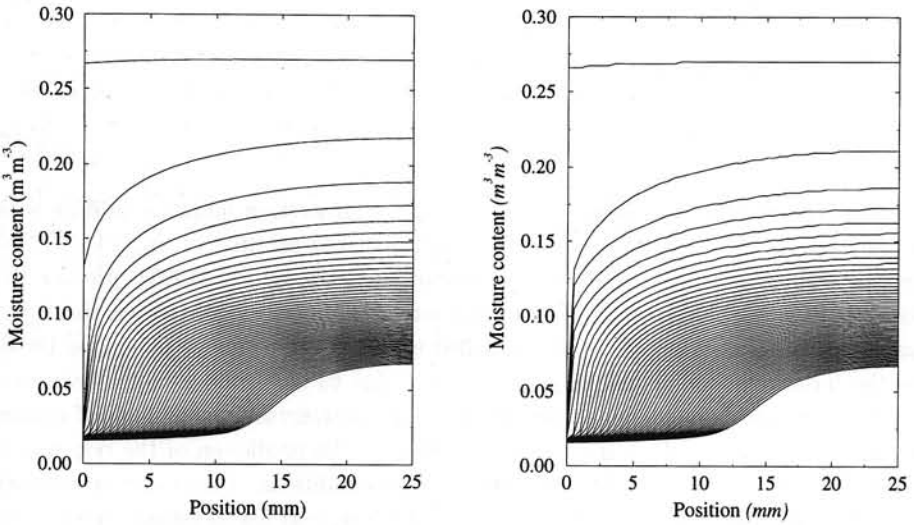

Figure 4.4: Moisture profiles obtained by FE solution of the nonlinear diffusion equation (a) for moisture content θ and (b) pore humidity h, moisture content subsequently being calculated from the hygroscopic relation $\theta(h)$.

Chapter 5

SIMULATION OF MASONRY CREEP AND SHRINKAGE EXPERIMENTS

To apply and validate the numerical formulation for moisture migration elaborated in the previous chapters, masonry drying experiments are analysed in this chapter. As the mechanical response in terms of shrinkage and creep serves as further verification and validation of the diffusion model, as well as the decoupled diffusion/mechanical modelling approach, it is analysed employing the mechanical model described in the accompanying report (Van Zijl 1999).

Recently Van der Pluijm and Wubs (1996) performed creep and shrinkage experiments on several of the most commonly used masonry combinations in The Netherlands. Compressive loads were applied, where as tensile creep behaviour would be of particular interest for the current study. Nevertheless, the experimental data serves as a valuable preliminary source for parameter estimation and computational model validation. Two masonry specimens, namely the calcium silicate element (KZE) and Waal Format (WF) brick specimens (KZB) respectively, Figure 5.1a, are studied here. Note that symmetry is assumed, requiring one-eighth of the specimens to be modelled, Figure 5.1b. This is clearly not the case for KZE, but the reduced computational effort justifies this simplification. It is believed that the sensitivity to this simplification of the global response in terms of total dimensional change in time is insignificant compared with the crudeness of the parameter estimation enforced here by insufficient experimental data.

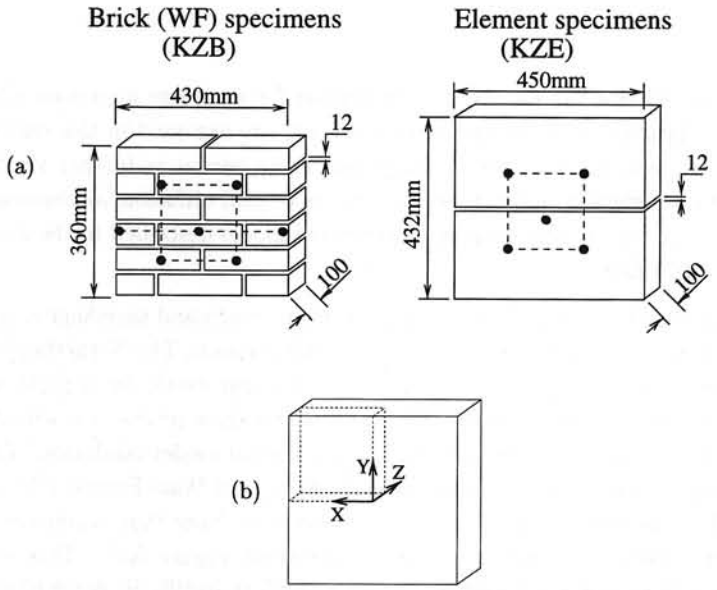

Figure 5.1: (a) Masonry shrinkage specimens investigated. (b) One eighth of each specimen modelled by assumption of symmetry.

5.1 Modelling approach

To investigate the moisture gradients and the resulting nonuniform dimensional change causing eigenstressing in the specimens, three-dimensional analyses are performed. In Appendix C the deficiency of plane (two-dimensional) modelling in capturing the slow drying response of a typical cementitious material is illustrated.

As outlined in the accompanying report (Van Zijl 1999) we can follow either a *discrete*, or a *macro/continuous* approach to model the masonry mechanical behaviour in two dimensions, more specifically, in the framework of plane stress. For three-dimensional analysis, however, discrete analysis is currently the only option, as the extension of the plane stress anisotropic Rankine continuum model (Lourenço 1996, Van Zijl 1999) to three dimensions is neither simple nor within the scope of this project. Thus we perform discrete analyses in this report, employing the three-dimensional interface model comprising a tension cut-off and Coulomb friction criterion based in multi-surface plasticity to capture nonlinear behaviour (cracking and shearing) in the brick-mortar interfaces, or the joint as a whole.

5.2 Model parameters: moisture migration

Pel (1995) performed NMR measurements of moisture profiles during drying of sand-lime specimens, similar to the calcium silicate material bricks/blocks used for the specimens tested by Vân der Pluijm and Wubs (1996). The diffusion coefficient derived from the moisture profiles via eq. (4.1) and the receding drying front method (Pel 1995) are assumed for the current analyses. The required hygroscopic relation $\theta(h)$ is also obtained from Pel (1995).

Furthermore, Pel measured moisture profiles in a typical masonry mortar, but cured in and subsequently taken from baked clay brick masonry. This procedure ensures that the mortar properties, as significantly influenced by the particular brick/block it is contact with, are measured. As no other mortar drying data is currently available, the diffusivity and hygroscopic curves measured by Pel are employed here. With regard to moisture loss this assumption is justifiable, because the total mortar volume in especially the KZE specimen is relatively small. However, the influence on the nonuniform shrinkage field and, accordingly, eigenstressing and cracking in the shrinking masonry specimen, is not easy to predict. The diffusion coefficient and hygroscopic curves employed are shown in Figure 5.2a,b respectively.

The surface convection coefficient (also known as film coefficient) is assumed as 5 mm/day for zero air speed (Tammes and Vos 1984). It turns out that the global drying response is insensitive to this coefficient in the range $0.5 \leq \beta < \infty$ mm/day - see section 5.9.1. However, employing a finite coefficient (5 mm/day) helps prevent overshoot - see Appendix D. Note that surface convection was modelled only at the wall face, because the edges of

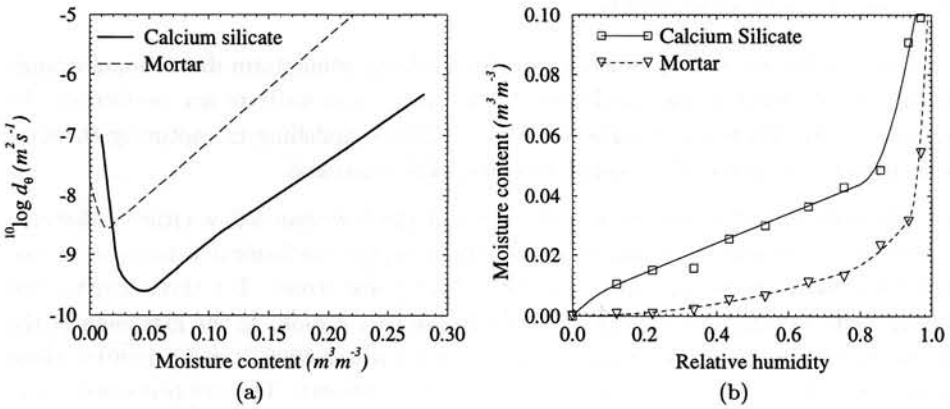

Figure 5.2: (a) Diffusion coefficient variation with moisture content and (b) isothermal desorption curves (Pel 1995).

each specimen were sealed in the experiments.

5.3 Model parameters: mechanical behaviour

The parameters needed to describe the mechanical behaviour are summarised in Tables 5.1 and 5.2. These parameters are based on the experimental studies by Van der Pluijm and Vermeltfoort (1991) and Van der Pluijm (1992) and have recently been verified thoroughly (Van Zijl 1996 and Van Zijl et al. 1997).

The Maxwell creep model parameters were obtained (Van Zijl 1999) by least squares curve fitting of measured compressive creep data by Van der Pluijm and Wubs (1996) - Figure 5.3.

Their creep specimens were subjected to a constant load, causing an average compressive stress of 2.5 N/mm^2. They measured shrinkage strains on *free shrinkage* specimens and approximated the *basic* creep ε_c, i.e. creep on non-drying specimens, by subtracting the free shrinkage ε_s and elastic strains ε_e as follows:

$$\varepsilon_c = \varepsilon - \varepsilon_e - \varepsilon_s \tag{5.1}$$

with ε the total strain measured on the drying creep specimens and ε_s the total strain measured on the drying, non-loaded specimens. This method ignores not only the influence of the stress level on the shrinkage strain, but also the influence of cracking due to *eigenstressing* in the free shrinkage specimens. Nonetheless, this data is used for a first estimate of the bulk creep parameters here.

Brick				Mortar		Interface					
E $\frac{N}{mm^2}$	ν	f_t $\frac{N}{mm^2}$	G_f^I $\frac{N}{mm}$	E $\frac{N}{mm^2}$	ν	f_t $\frac{N}{mm^2}$	G_f^I $\frac{N}{mm}$	c_o $\frac{N}{mm^2}$	$\tan\phi_o$	$\tan\phi_r$	G_f^{II} $\frac{N}{mm}$
11500	0.2	2.0	0.06	3300	0.2	0.1	0.005	0.28	0.97	0.75	0.02-0.03σ

Elasticity			Strength			Softening		
E	=	Young's modulus	f_t	=	tensile strength	G_f^I	=	tensile fracture energy
ν	=	Poisson's ratio	c_o	=	original adhesion	G_f^{II}	=	shear fracture energy
			ϕ_o	=	initial friction angle	σ	=	normal stress (N/mm^2)
			ϕ_r	=	residual friction angle			

Table 5.1: Mechanical material parameters employed for calcium silicate brick and element specimens.

$\tan\psi_o$	σ_u $\frac{N}{mm^2}$	δ
0.67	-1.22	17

$$\Psi = \frac{\Delta u}{\Delta v} = \tan\psi_o \left(1 - \frac{\sigma}{\sigma_u}\right) e^{-\delta\,\Delta v}$$

Ψ	=	dilatancy coefficient	ψ_o	=	dilatancy angle at zero pressure and shear-slip
Δu	=	uplift normal to joint	σ_u	=	pressure inhibiting any uplift
Δv	=	shearing along joint	δ	=	gradient of surface smoothing with shear-slip

Table 5.2: Dilatancy parameters employed.

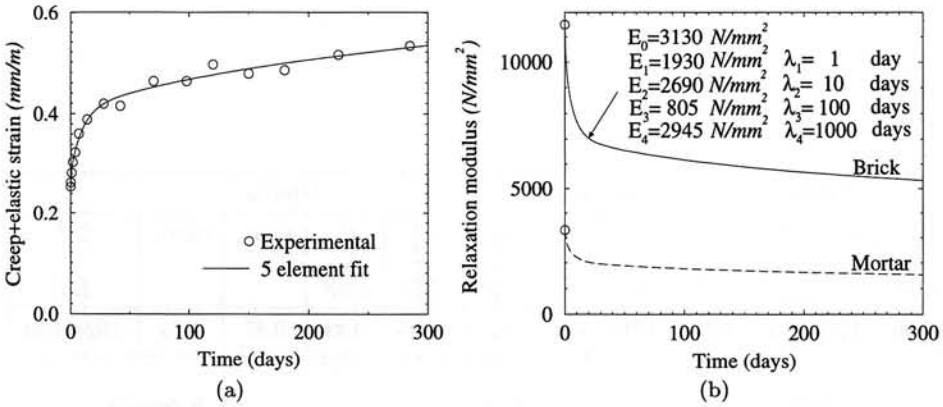

Figure 5.3: (a) Measured creep and fitted five-element Dirichlet function. (b) Relaxation function derived from (a).

Nearly equal creep coefficients, defined as

$$\phi_c = \frac{\varepsilon_c}{\varepsilon_e}, \tag{5.2}$$

were reported for the KZE and KZB specimens. Equal creep coefficients are assumed for the bricks, elements, as well as the mortar. This means that the same relaxation times $(\lambda_1, \lambda_2, ...\lambda_N)$ are used for both constituents and, once the Maxwell spring stiffnesses $(E_1, E_2, ..., E_N)$ have been found for one constituent, those for the other are obtained by mere factorisation:

$$E_{n,m} = \frac{\sum_{n=1}^{N} E_{n,m}}{\sum_{n=1}^{N} E_{n,b}} E_{n,b} = \frac{E_m}{E_b} E_{n,b} \tag{5.3}$$

where the subscripts m and b refer to mortar and brick respectively. Aging is not considered, despite evidence of masonry compressive creep aging (Shrive et al. 1997).

As outlined in Van Zijl (1999), the shrinkage strain is related to the pore humidity by the shrinkage coefficient (α_s) in an incremental fashion:

$$\mathrm{d}\boldsymbol{\varepsilon_s} = \alpha_s \left(\boldsymbol{P} - \boldsymbol{r\sigma}\right) \mathrm{d}h \tag{5.4}$$

where

$$\boldsymbol{P} = [\, P_x \;\; P_y \;\; P_z \;\; 0 \;\; 0 \;\; 0 \,]^T$$

$$\boldsymbol{r} = \begin{bmatrix} r_x & \cdot & \cdot & \cdot & \cdot & \cdot \\ \cdot & r_y & \cdot & \cdot & \cdot & \cdot \\ \cdot & \cdot & r_z & \cdot & \cdot & \cdot \\ \cdot & \cdot & \cdot & \cdot & \cdot & \cdot \\ \cdot & \cdot & \cdot & \cdot & \cdot & \cdot \\ \cdot & \cdot & \cdot & \cdot & \cdot & \cdot \end{bmatrix}. \tag{5.5}$$

$\boldsymbol{P}$ provides for different free shrinkage coefficients in orthogonal directions, and $\boldsymbol{r}$ provides for the orthotropic normal stress-dependence of shrinkage. The coefficients which reflect the *apparent* stress-dependence of shrinkage, r, should be determined by performing simultaneous *drying creep*, *basic creep* and *free shrinkage* tests. The discrepancy between drying creep on the one hand and the superposition of basic creep and free shrinkage on the other hand, quantifies r. In the absence of such data, these coefficients are set to zero.

The measurement of true shrinkage, i.e. the volume reduction of a material element at zero stress, is virtually impossible, hampered by the slow drying process in cementitious materials which causes humidity gradients, eigenstresses and cracking. Therefore, direct determination of the shrinkage coefficient is hardly possible. Furthermore, tests by Alvaredo et al. (1995) indicate that for cement paste of various water/cement (w/c) ratios, the coefficient depends on the relative humidity, as will be discussed in detail in section 5.9.2. As a first approach constant shrinkage coefficients are assumed. If, in addition, one ignores the influences of cracking and stress-dependence of shrinkage ($\boldsymbol{r} = \boldsymbol{0}$ in eq. 5.4), the coefficients can be estimated from the "final" shrinkage strain (ε_s^∞). This is done by solving the differential equation (5.4) with initial condition $\varepsilon_s(0) = 0$:

$$\varepsilon_{s,i} = \alpha_s \, P_i \, (h - h_o) \tag{5.6}$$

and substituting the "final" shrinkage strain (ε_s^∞) and environmental humidity (h_E) as follows:

$$\alpha_s \, P_i = \frac{\varepsilon_s^\infty}{(h_E - h_o)}. \tag{5.7}$$

The shrinkage parameters calculated in this manner are listed in Table 5.3. Note that, due to the absence of separate shrinkage data for the mortar and the bricks, the coefficients derived from the *masonry* data are assumed and employed for each constituent in the discrete analyses.

specimen	α_s	P_x	P_y	P_z
large block	0.000525	1.0	1.2	1.0
WF	0.0007	1.0	1.08	1.0

Table 5.3: Shrinkage coefficients derived from final shrinkage strain values of masonry shrinkage specimens.

5.4 Spatial and time discretisation

It is well known that care should be taken with spatial and time discretisation, with regard to the numerical solution of both the diffusion equation and mechanical behaviour. To avoid numerical *overshoot* of the pore humidity, time steps should be not too small, while the elements should be small close to surface and other phase boundaries. At the same time step sizes should be limited to avoid large humidity-time gradients. Here, time steps were chosen to restrict increments in humidity to $\Delta\ h \approx 0.025$. This gives time steps for the diffusion analyses of one half hour initially and up to 20 days towards the end of the test period (200-300 days). For the mechanical analyses the time steps are roughly one quarter of those for the diffusion analyses to ensure accuracy and avoid convergence problems. In Appendix D the issue of *overshoot* is illustrated.

The spatial discretisation is equally important. The overshoot is attenuated by a too coarse mesh. The non-smoothness of the diffusion equation coefficients contributes to the requirement for dense FE meshes, as is illustrated in Appendix B. Furthermore, by intelligent discretisation in areas of large shrinkage strain gradients, i.e. in the thickness direction, the gradient per element can be minimised, ensuring the most accurate representation of the stress and strain fields for a given mesh density. This is illustrated by Figure 5.4, where the pore humidity evolution is shown at points through the specimen thickness for uniform, Figure 5.4a, and nonuniform discretization, Figure 5.4b, through the thickness. In the nonuniform case element sizes in the thickness direction increase with a factor two from the surface inwards.

5.5 Boundary conditions and initial values

The experiments were conducted at a controlled climate of 50% humidity and 20°C. For a zero air flow velocity a surface convection transfer coefficient (2.12) of $\beta = 0.025$ s/μm is appropriate (Tammes and Vos 1984). This gives a film coefficient of:

$$\beta = \frac{\beta^*\ p_s}{\rho_l} = \frac{0.025.10^{-6} \times 2338}{1000} = 0.058\ \ \mu\text{m/s}\ \text{ or }\ 5\ \ \text{mm/day}$$

The calcium silicate bricks and elements were pre-wetted to a moisture content of between 6% and 8% by mass, according to standard building procedure for this material (Van der Pluijm and Wubs 1996). The total weight was measured at each time of shrinkage and

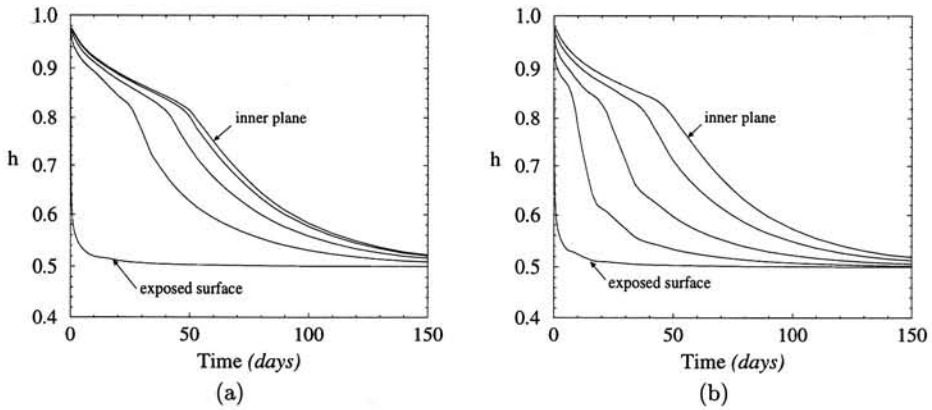

Figure 5.4: Humidity evolution at points through the masonry specimen thickness for (a) uniform and (b) nonuniform spatial discretisation in the thickness direction.

creep strain measurement. After the experiments the dry weight of the specimens was measured, enabling the average moisture content at any time during the experiment to be calculated. In this manner the initial moisture content in the large block and WF specimens was calculated to be 6.5% and 8.0% respectively. To convert the initial moisture content to initial pore humidity two assumptions need to be made. Firstly, the interfaces between brick and mortar are assumed to be hydraulically perfect, meaning that the pore humidity is continuous across them. Secondly, the pore humidity is assumed to be uniform initially in the mortar and bricks in each specimen. This initial value can then be calculated which, by considering the respective hygroscopic curves, corresponds with the total initial moisture content. This calculation leads to $h_o = 0.96$ for the large block specimen (KZE) and $h_o = 1.0$ for the WF specimen (KZB).

5.6 Results: Calcium silicate element (KZE) specimen

Figure 5.5a-d show the numerical pore humidity contours at various stages of drying of the KZE specimen. Good agreement is obtained with the measured moisture content in time, Figure 5.5e.

By inspection of the humidity contours, it can be seen that the exposed surface is nearly in equilibrium with the environment after one day. However, due to the low diffusivity the bulk of the specimen remains saturated, causing large gradients through the depth, especially close to the exposed surface. The gradients gradually reduce until equilibrium is reached with the environment after about 100 days of drying.

Figures 5.6a-d show the maximum principal *eigenstresses* accompanying the hygral gradients in the free drying specimen. In the early stages high tensile stresses occur at the surface, causing initiation of debonding. The brick strength (2 MPa) is also slightly exceeded in the brick faces, so that some drying cracks could initiate and grow there, but this fact is ignored in our modelling strategy. As time passes the peak stresses reduce along with the hygral gradients until a virtually (eigen)stress-free state is reached after 100 days. Note that the deformations have been scaled up by a factor of 1000. The maximum crack width is in the order of 7μm, reached after ten days.

Figure 5.6e shows that reasonable agreement is obtained between the measured and numerical average strains in the gauge length in the x direction, as well as in the y direction. The dashed line shows the numerical result if the debonding at the interfaces is not modelled.

When a vertical (y-direction) compressive creep pressure of -2.5 N/mm^2 is applied simultaneously in order to simulate the drying creep experiment, the tensile eigenstresses are offset sufficiently to prevent cracking. In Figure 5.7 the numerical *drying* and *basic* creep strains are compared with the experimental data. The basic creep is obtained by subtracting the free shrinkage strain, Figure 5.6e, from the total strain in the gauge length on the drying creep specimen. Note that the creep experiments were only performed in the y-direction.

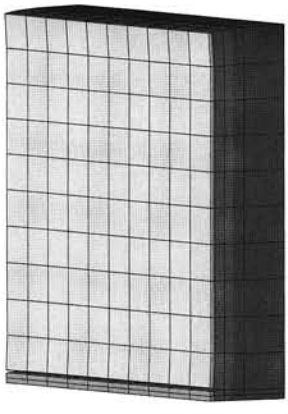

(a) 1 day:

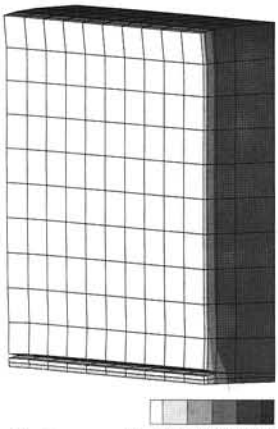

(b) 10 days:

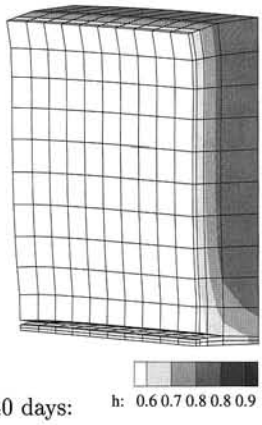

(c) 40 days:

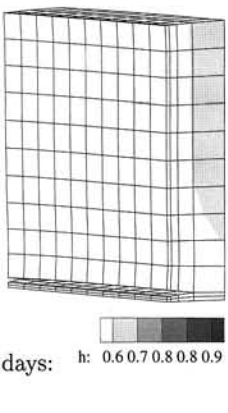

(d) 100 days:

(e)

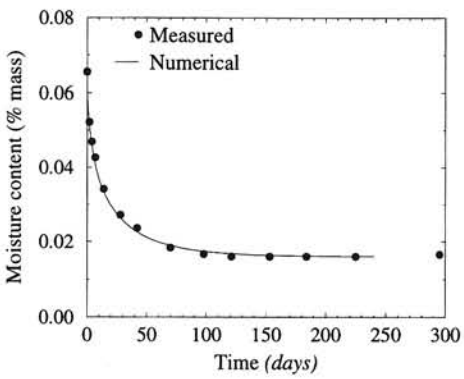

Figure 5.5: (a-d) Pore humidity contours and (e) moisture content (% by mass) evolution in drying single joint calcium silicate (KZE) specimen.

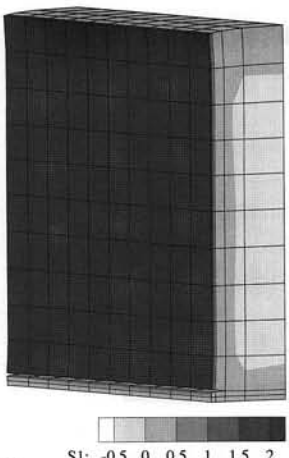

(a) 1 day:

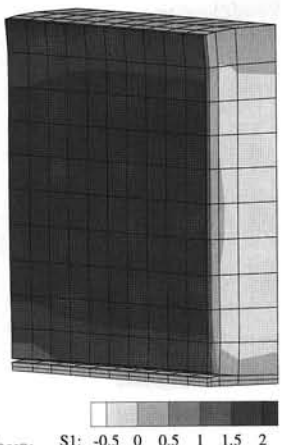

(b) 10 days:

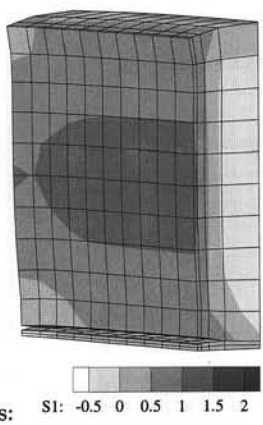

(c) 40 days:

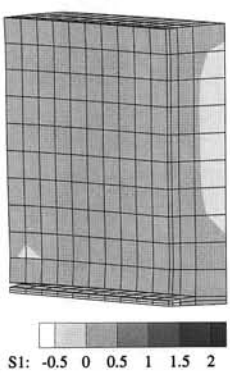

(d) 100 days:

(e)

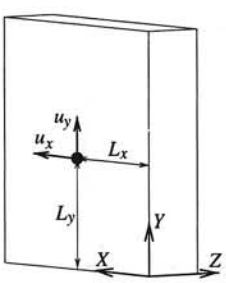

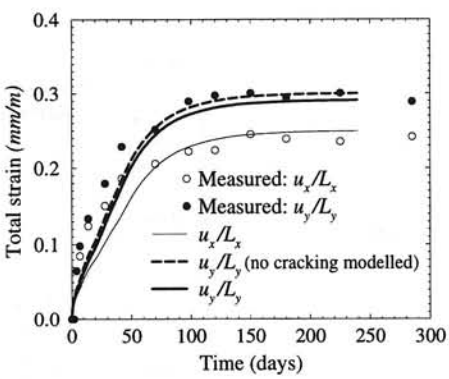

Figure 5.6: (a-d) Contours of maximum principal stress and (e) total strain in the gauge length in *free* drying single joint calcium silicate (KZE) specimen.

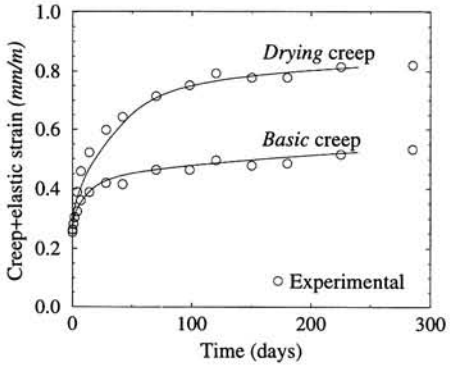

Figure 5.7: KZE *drying* and *basic* creep response.

5.7 Results: Calcium silicate brick (KZB) specimen

5.7.1 Assumed moisture migration parameters

It is well known that the calcium silicate elements and WF bricks exhibit quite different behaviour (Van der Pluijm and Wubs 1996). In the above section it was shown that the parameters taken from Pel (1995) give reasonable agreement with the KZE measured moisture loss and shrinkage response. This is not so for the WF specimen. Having no experimental data for WF specimen specifically, the Pel (1995) parameters were modified to obtain better agreement. Firstly, the desorption curve was adjusted, Figure 5.8a, to give the same residual moisture content (2% by mass) in the KZB specimen at the environmental humidity (50%) as measured by Van der Pluijm and Wubs (1995). Secondly, the diffusion coefficient was taken as one tenth of the measured value, Figure 5.8b, to simulate the drying rate better.

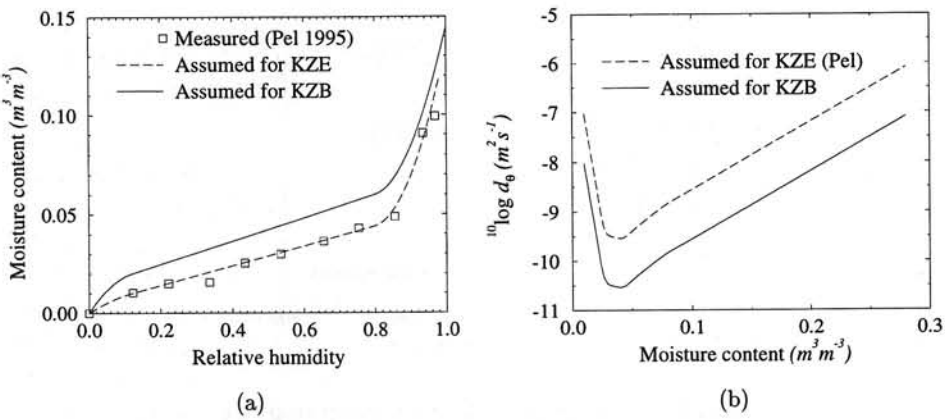

Figure 5.8: Assumed (a) desorption curve and (b) diffusion coefficient for the calcium silicate WF specimen.

5.7.2 KZB results for the assumed moisture migration parameters

Figure 5.9e shows the measured moisture contents and those found with and without the above adjustments. It must be stressed that these modifications were made simply to fit the measured drying response better. They do not exhaust the possible differences in the comprising materials of the KZE and KZB specimens.

Also shown in Figure 5.9 are the pore humidity profiles at various stages of drying. After one day large gradients exist through the depth close to the exposed surface. Large humidity gradients also occur between the mortar and bricks, due to the different hygroscopic relations of the two constituents. Because of the higher diffusivity, the mortar dries

quicker than the bricks, yet the pore humidity in the mortar reduces at a lower rate. The gradients reduce until equilibrium is reached with the environment after about 100 days of drying.

Figures 5.10a-d show the maximum principal *eigenstresses* accompanying the hygral gradients. In the early stages high tensile stresses occur at the surface, causing initiation of debonding. The brick strength (2 MPa) is also slightly exceeded in the brick faces, so that drying cracks could develop there, but this fact is ignored in our modelling strategy. As time passes the peak stresses reduce along with the hygral gradients until a virtually (eigen) stress-free state after 100 days. Note that the deformations have been scaled up by a factor of 500. The maximum crack width is in the order of 7μm, reached after ten days.

Figure 5.10e shows that reasonable agreement is obtained between the measured and numerical average strains in the gauge length in the x direction, as well as in the y direction. If the debonding at the interfaces is not included in the model, a significantly larger shrinkage, the dashed line in Figure 5.10e, is obtained in the y direction, where 3 delaminating interfaces are included in the gauge length. As the shrinkage parameters have been estimated ignoring the influence of cracking, the uncracked numerical response represents the experimental response well.

The response to the 2.5 N/mm^2 compressive creep load is shown in Figure 5.11, where the deformations have been scaled up with a factor of 375. Splitting is initiated along the vertical interfaces in response to the creep load, which is assumed to be applied linearly over a period of 5 minutes. Subsequently the superimposed *eigenstresses* cause the splitting cracks to open wider, while the debonding along the horizontal interfaces seen in the case of the free drying KZB specimen is prevented by the compressive creep load. The *basic* creep strains are obtained by subtracting the free shrinkage strain, Figure 5.10e, from the total strain in the gauge length on the drying creep specimen, Figure 5.11e.

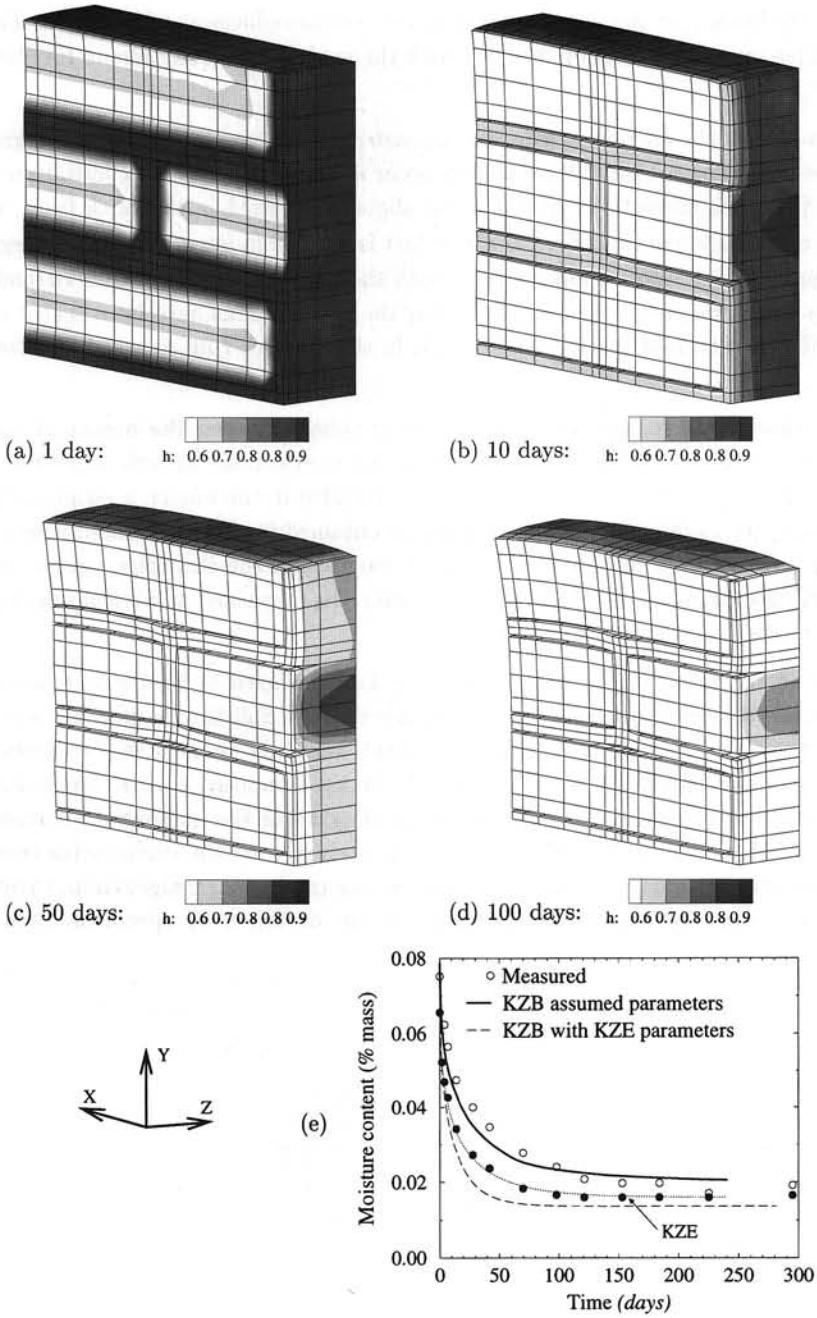

Figure 5.9: (a-d) Pore humidity contours and (e) moisture content (% by mass) evolution in drying WF calcium silicate (KZB) specimen.

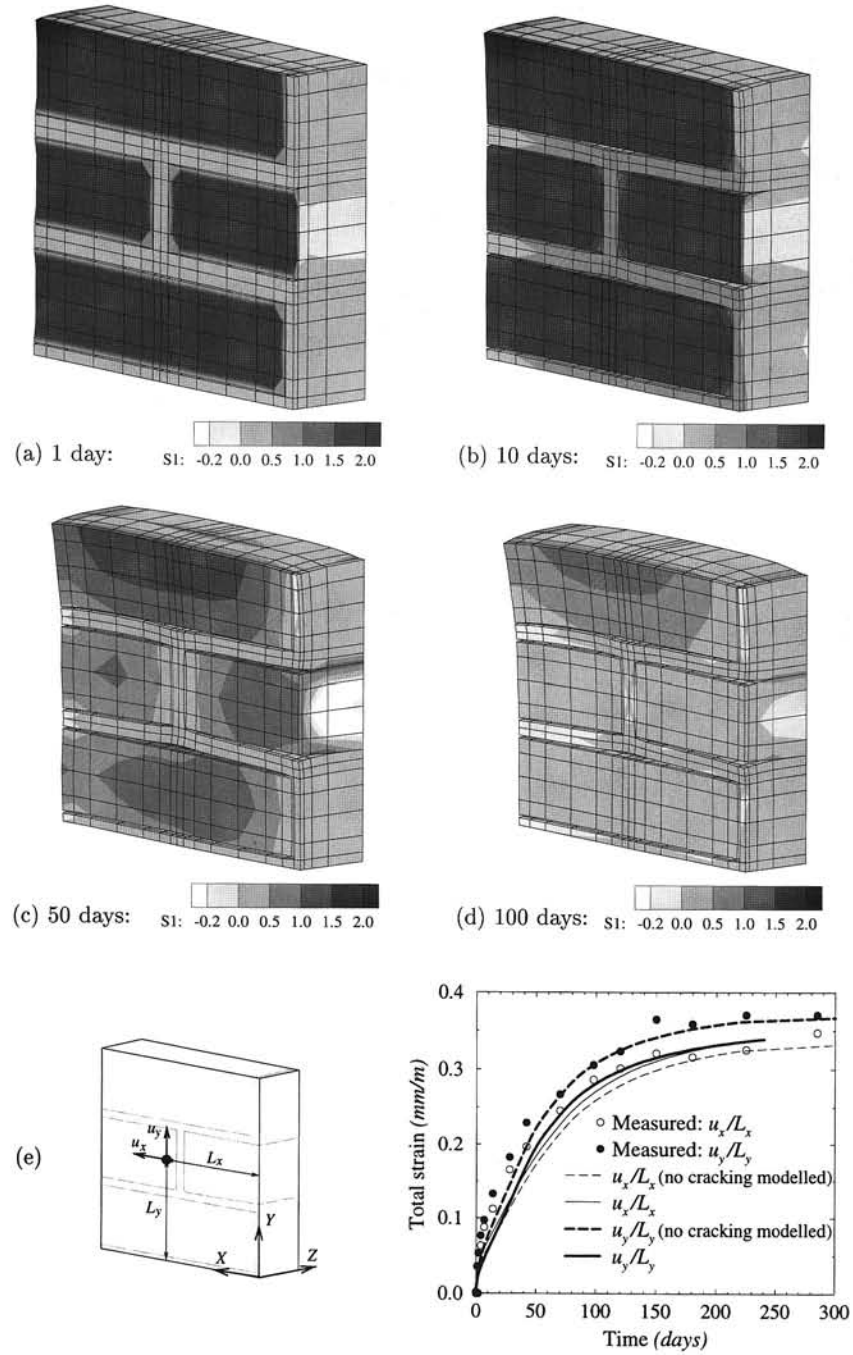

Figure 5.10: (a-d) Contours of maximum principal stress and (e) total strain in the gauge length in *free* drying WF calcium silicate (KZB) specimen.

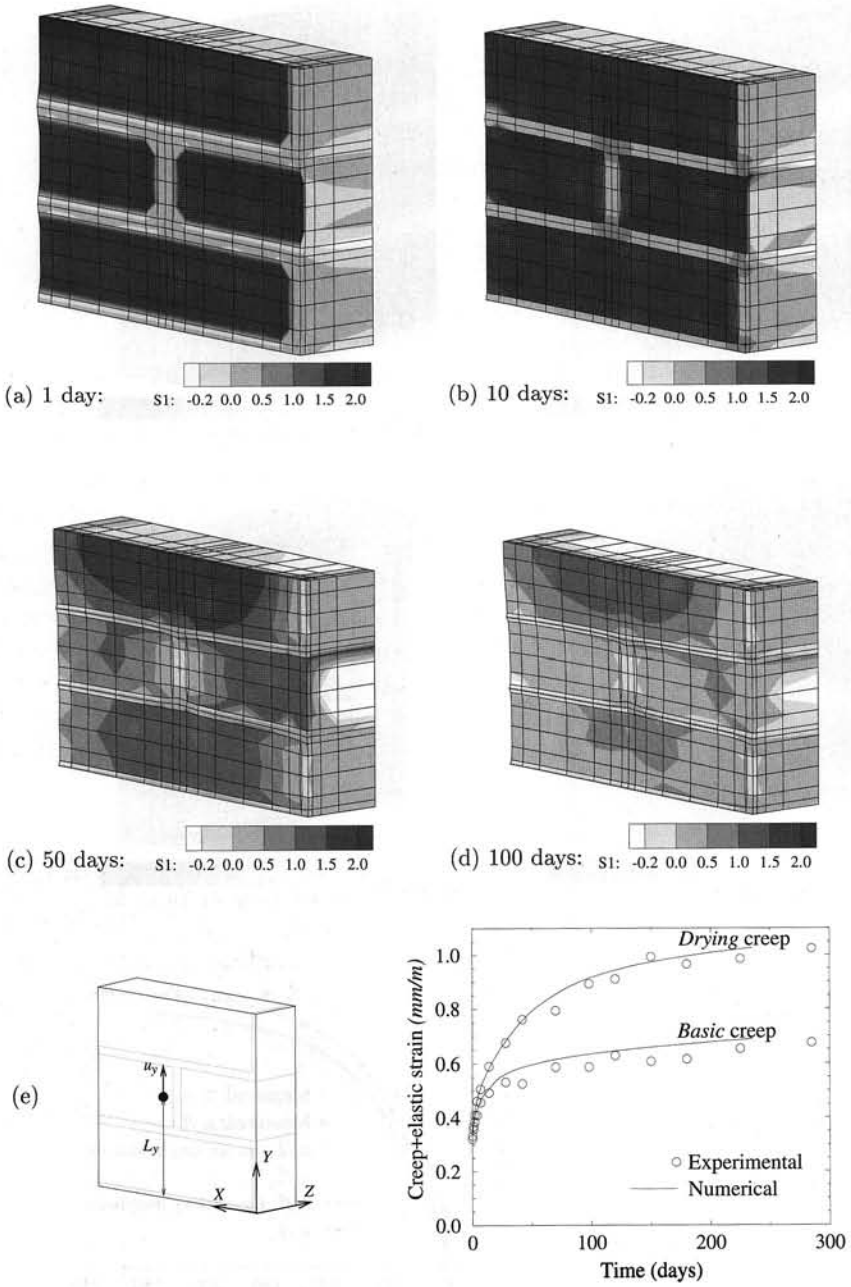

Figure 5.11: (a-d) Contours of maximum principal stress in KZB drying creep specimen. (e) Total strain (y direction) in the gauge length in KZB creep specimen subjected to shrinkage (*drying creep*) and with free shrinkage subtracted (*basic creep*).

5.8 Mesh objectivity

The free shrinkage KZB specimen was analysed with the three meshes shown in Figure 5.12.

The global behaviour, as reflected by total moisture content (by mass) and total strain, as calculated from the total displacement at the gauge point at the surface, see for example Figure 5.11e, is shown in Figure 5.13. The response converges with mesh refinement.

Furthermore, oscillating stress fields may occur when employing the same interpolation order for pore humidity and displacement, as was done in the above analyses. This is because the linear shrinkage strain variation in each eight-noded brick element obtained from the diffusion analysis, has to be represented by the constant strain capacity of this element in the mechanical analysis. However, in the three-dimensional analyses performed here, equal-order interpolation of pore humidity and displacements produces compatible strain fields in the orthogonal directions. For instance, the normal strain component ε_x is constant in the x-direction, but linear in the orthogonal directions in the eight-noded brick. To verify that a multi-dimensional analysis with equal-order interpolation does indeed cause less pronounced disturbance in the stress fields, the KZB free shrinkage case was re-analysed with mesh 2, but employing twenty-noded bricks. In terms of countours of principle stresses no significant difference between the linear element and quadratic element results was found. A more detailed study of stress component fields should be performed to investigate the existence and extent of stress oscillations. However, the global deformational response matched the eight-noded mesh 2 response, Figure 5.12,

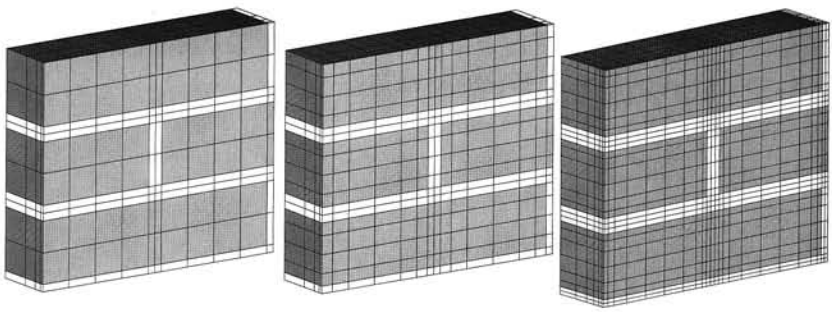

	Mesh 1	Mesh 2	Mesh 3
Bricks (LxH)	4x2	6x4	9x6
Total (LxHxD)	11x11x4	15x17x4	23x26x6
Total	484	1020	3588

Figure 5.12: Finite element meshes employed to investigate mesh objectivity of the numerical simulation of the KZB shrinkage specimen.

with an insignificant improvement in the early stages. To avoid excessive computational effort mesh 2 with eight-noded elements has been employed for all the KZB analyses reported.

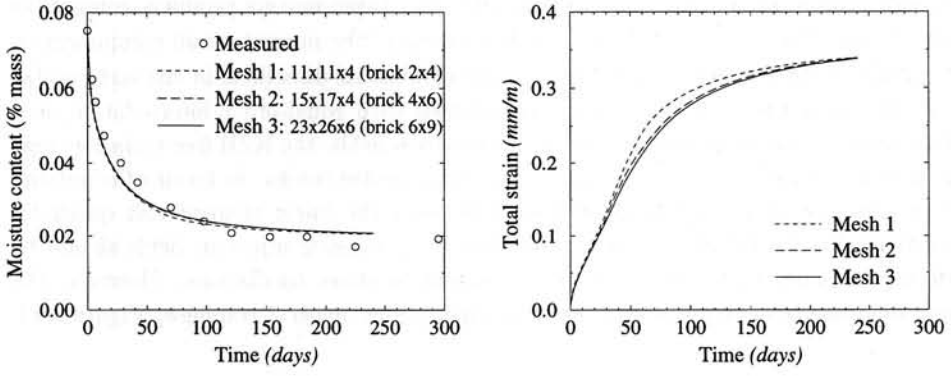

Figure 5.13: (a) Moisture content (by mass) and (b) total strain in the gauge length for the three meshes employed, Figure 5.12.

5.9 Sensitivity study

Having only experimental data on the meso-scale available for estimation of the model parameters, some quantification of the sensitivity to the estimation error is required.

5.9.1 Moisture content dependence on surface convection coefficient

The film coefficient β is dependent mostly on wind speed and surface roughness. As mentioned in section 5.2 a coefficient of 5mm/day was assumed to simulate the zero wind velocity in the experimental environment. To evaluate the sensitivity to this parameter, two extreme cases were analysed additionally, namely for $\beta = 0.5$ and $\beta = \infty$ mm/day. The infinite film coefficient is modelled by setting the surface humidity equal to the environmental humidity. In Figure 5.14 the evolution of the total moisture content by percentage of mass is shown for the three cases. The global drying response is clearly insensitive to the film coefficient, but, as shown in Appendix D, a finite value sufficiently slows down surface drying to prevent overshoot near the surface.

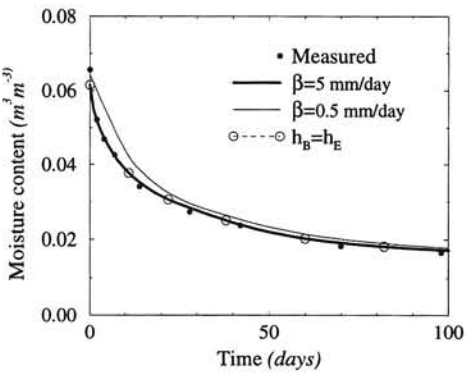

Figure 5.14: Influence of surface convection coefficient on masonry moisture content.

5.9.2 Shrinkage coefficient dependence on humidity

As discussed in section 5.3, a constant coefficient of shrinkage α_s was estimated from the "final" shrinkage strain obtained from the drying tests. However, a strong dependence on the relative humidity has been reported by Alvaredo et al. (1995). Their tests indicate that for cement pastes of various water/cement (w/c) ratios, the coefficient depends on the relative humidity, as summarised in Table 5.4. To study the sensitivity of masonry

	α_s ($\times 10^{-3}$)	
	w/c=0.4	w/c = 0.5
$0.75 < h < 1.00$	1.5	2.3
$0.60 < h \leq 0.75$	0.7	0.2
$0.45 < h \leq 0.60$	0.1	0.5

Table 5.4: Shrinkage coefficients derived from final shrinkage values of cement pastes at different environmental humidities (Alvaredo et al 1995).

shrinkage to the variation of α_s with humidity, also a linear and a parabolic relation have been employed. The relations reflect the "final" shrinkage strain, as derived from:

$$\int \dot{\varepsilon}_s dt = \int \alpha_s(h)\dot{h}dt + \text{constant} \tag{5.8}$$

with

$$\alpha_s(h) = \begin{cases} a \\ a\,h \\ a\,h^2 \end{cases} \quad \Rightarrow \quad a = \begin{cases} \dfrac{\varepsilon_s^\infty}{h_E - h_o} \\ \dfrac{2\varepsilon_s^\infty}{h_E^2 - h_o^2} \\ \dfrac{3\varepsilon_s^\infty}{h_E^3 - h_o^3} \end{cases} . \tag{5.9}$$

Figure 5.15 shows that better agreement is obtained with the measured shrinkage when considering humidity dependence of the shrinkage coefficient.

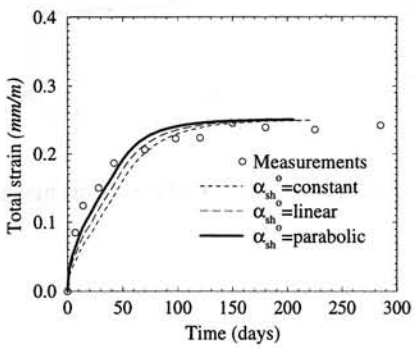

Figure 5.15: Influence of shrinkage coefficient dependence on humidity on *free* shrinkage.

5.9.3 Pickett effect

No experimental data is available from which the shrinkage stress-dependence coefficients r_x, r_y and r_z in eq. (5.5) can be estimated. As discussed by Van Zijl (1999), they have been shown to be in the range $0.2/f_t \leq r_i \leq 0.8/f_t$. The KZE specimen was re-analysed for the two extreme, isotropic cases. Figure 5.16a shows the free shrinkage strain distribution through the thickness at the gauge point after 30 and 120 days of drying. The corresponding vertical stress components are shown in Figure 5.16b, revealing a relaxation effect of the stress-dependence coefficient. Where as cracking is expected also in the blocks and bricks for $r_i f_t = 0$ (sections 5.6, 5.7.2), the maximum coefficient ($r_i f_t = 0.8$) reduces the stresses to within the calcium silicate block and the WF brick tensile strength. However, it has only an insignificant influence on the observed strain of both the free drying KZE and KZB specimens. When the creep load acts, a significant influence is seen, Figure 5.17. The total compressive strain is increased by up to 30%, which means that, if such a dependence does exist, the experimentally measured *basic* creep is over estimated, because it contains the stress-dependent shrinkage strain component not reflected by the free shrinkage. Only by testing similar, but non-drying creep specimens the error can be quantified.

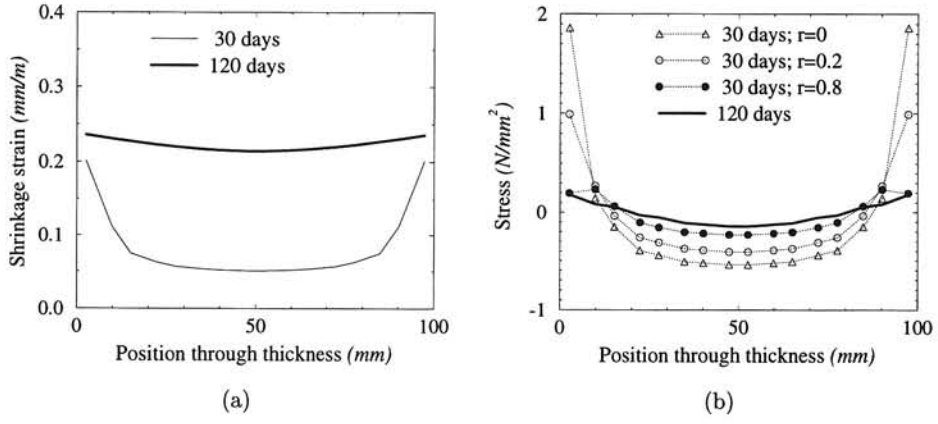

Figure 5.16: (a) "Free" shrinkage evolution and (b) stress distribution through the thickness at the gauge point in the KZE specimen.

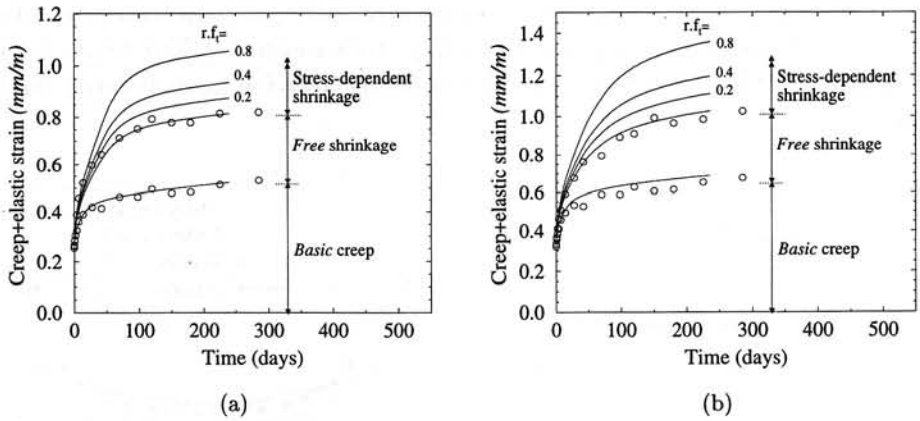

Figure 5.17: Illustration of Pickett-effect in (a) KZE and (b) KZB creep specimen.

5.9.4 Creep/relaxation

A variation in the creep modelled is obviously directly translated into increased or decreased total deformation in creep analyses. However, if the free shrinkage response is sensitive to the assumed creep parameters, an inverse process of parameter determination becomes more difficult. To investigate this sensitivity, both KZE and KZE specimens were re-analysed with no bulk creep. The case of $\boldsymbol{r} = \mathbf{0}$, i.e. zero Pickett effect, was analysed. Figure 5.18 shows the influence of bulk creep on the free drying shrinkage. If bulk creep is included in the model, a significantly larger total vertical deformation is found at the gauge point(KZE +3%, KZB +9%), but a decrease in maximum crack width (KZB, from 8.7μm to 7.5μm). Also, the maximum principal stress is relaxed by up to 20% in KZE and 12% in KZB.

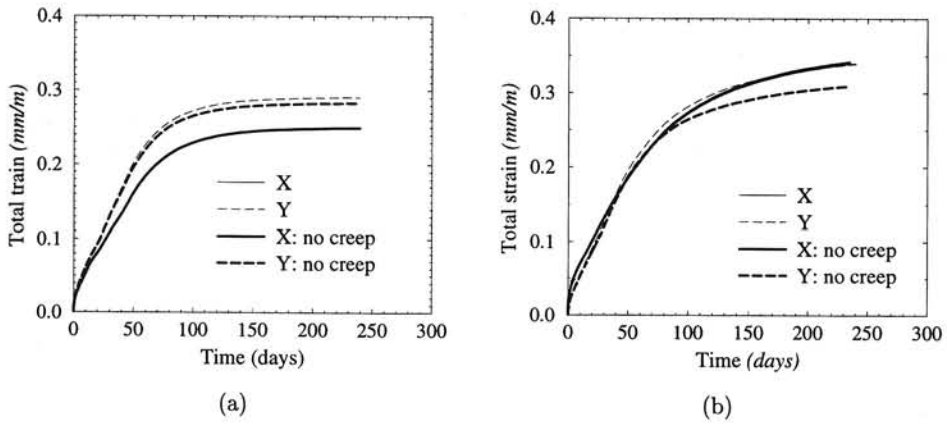

Figure 5.18: Influence of bulk creep on (a) KZE and (b) KZB masonry *free* shrinkage.

5.10 Discussion

From the numerical results presented in the above sections it is clear that the model parameters for time dependent behaviour cannot be derived directly from the available experimental data. The good agreement obtained with the measured moisture loss in the KZE specimen can be considered as coincidental, because the moisture migration parameters were obtained from measurements by a different research group on sand-lime material not unlike the blocks in the KZE specimens, but probably subjected to a different manufacturing process. This argument is strengthened by the large difference in moisture loss evolution found for the KZB specimen when employing the same (KZE) diffusion and hygroscopic parameters. Experimental determination of these material parameters for the block and WF calcium silicate units are necessary. Also, the moisture migration in the mortar taken from KZE and KZB type specimens should be characterised experimentally,

because, although exactly the same mortar is used for manufacturing KZE and KZB, the units strongly influence the properties of the cured mortar.

With regards to the mechanical behaviour, the difficulty in deriving the material parameters from the experimental data is due to the tests being on the *meso*-scale and, even more importantly, not carefully designed to distinguish between the various mechanisms. No information about stress-induced shrinkage ($\boldsymbol{r}$) can be derived from the data. It has been argued in section 5.9.3 that this leads to an over estimation of the *basic* creep if derived by subtracting the *free* shrinkage strain from the (compressive) *drying* creep. This is illustrated in Figure 5.19. Note that, for the purpose of illustration, the lower limit of $r = 0.2/f_t$ published for concrete has been employed to analyse the *drying* creep response. The stress-induced shrinkage should be subtracted to obtain a better estimate of the basic creep.

An additional source of error is also unveiled in the figure. Cracking reduces the material (stress-free) shrinkage in the free drying specimen, but does not occur in the creep specimen, the tensile stresses being offset sufficiently by the creep load. This effect should also be quantified to derive the basic creep. It can be done numerically by comparing the numerical results of the free shrinkage specimen with the response if the cracking criterion is ignored, i.e. no cracking is modelled. However, also in these analyses the basic creep modelled influences the response significantly, Figure 5.18 section 5.9.4, calling for an inverse approach.

Two alternative ways can be followed to find better approximations of the model parameters. The first involves an iterative numerical approach of adjustment of the model parameters and re-analysis until a satisfactory agreement between the numerical and experimental results has been obtained. In the above sections only the first iteration has

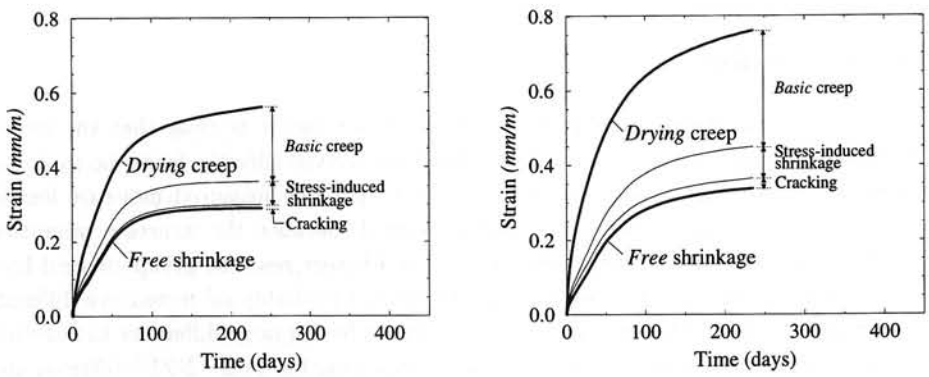

Figure 5.19: Determination of *basic* creep for (a) KZE and (b) KZB masonry.

been done. The second iteration would involve selection of:

- an increased shrinkage coefficient to allow for the reduction of the free shrinkage strain caused by cracking,
- smaller bulk creep, by selecting increased stiffnesses for the Maxwell elements, to allow for stress-induced shrinkage in the drying creep specimen and cracking in the free shrinkage specimen.

However, information about the stress-dependence of the shrinkage is lacking. Also, the moisture migration in the different comprising materials must be characterised, calling for a new set of experiments. This causes the second approach, a carefully designed experimental program, which addresses all known mechanisms, to be favoured. Such a program is proposed in Chapter 6.

Here, tensile creep is of importance. In tensile creep tests cracking may occur in all three specimens (the free shrinkage, basic creep and drying creep specimens), but to a varying degree. It is possible to design the experiments and specimens to avoid cracking in the gauge area, as discussed in Chapter 6. Bažant and Xi (1993) have proposed bending experiments from which results the contribution of cracking can be distinguished. However, bending tests introduce additional difficulties, especially when dealing with masonry.

Chapter 6

EXPERIMENTAL PROGRAM: PROPOSAL

A small amount of data exists for characterisation of creep and shrinkage of masonry. As described in chapter 5, some parameters required to model these phenomena can be estimated from the existing data. However, to strive at accurately pin-pointing individual parameters included in the numerical model described in this report and the accompanying report (Van Zijl 1999), better and more discriminating experiments are needed. For instance, no data exists for estimating the influence of stress on the shrinkage, having received little attention by masonry researchers up to now. Also, the major masonry experimental focus has been on *compressive* creep. *Tensile* creep, a major role player in restraint of masonry shrinkage, will be studied here.

In this chapter a proposal for an experimental program is given to obtain specific data for characterisation of creep and shrinkage in typical Dutch masonry, Table 6.1. The details of the grading, preparation and application of the constituent materials, as well as the masonry fabrication procedures, are to be as described by Van der Pluijm and Wubs (1996) and will not be repeated here.

Combination	Brick/block type	Joint type
1 2	Calcium silicate brick	12 mm 1:1:6 mortar thin layer Calsifix glue
3 4	Calcium silicate block	12 mm 1:1:6 mortar thin layer Calsifix glue
5 6	Fired-clay brick	12 mm Beamix 316 mortar thin layer mortar Ankerplast
7 8	Concrete brick	12 mm Beamix 312 mortar thin layer mortar C62

Table 6.1: Typical Dutch masonry types to be tested.

Measurements on small specimens are described, sections 6.1 and 6.2, designed to minimise coupling between effects and thus to ensure objective derivation of model parameters . Simultaneously, larger specimen should be subjected to drying and creep loads for eventual verification of the parameters and validation of the modelling approach, section 6.3. The reason for simultaneous testing of small and large scale specimens is, apart from saving time, to have the opportunity of fabricating all specimens by the same laborants, under the same circumstances and of "identical" ingredients, delivered from the same batches.

6.1 Moisture migration

The parameters required for analysing the moisture migration in masonry are the diffusivity coefficient $D(\theta)$ and the hygroscopic relation $\theta(h)$. The former can be derived from the moisture profiles in one-dimensional wetting (absorption) and drying (desorption) tests on specimen of masonry constituents taken from cured masonry specimens by boring. Taking the samples from masonry ensures inclusion of synergy effects, for instance the microscopic change in the porosity of the mortar in the interface region due to fine particles transported by migrating moisture to and clogging the pores in this area, leading to lower mortar diffusivity. Nuclear Magnetic Resonance (NMR) provides a suitable way of measuring the moisture profiles, as described in detail by Pel (1995), section 4.2. The hygroscopic relation must be established by absorption and desorption tests of similar masonry constituent specimens at different levels of relative humidity, each time allowing enough time for equilibrium to be reached at the particular climate.

6.1.1 Moisture diffusivity

NMR measurement of moisture content profiles in drying brick/block specimens (type 1, Figure 6.1), mortar taken from the particular masonry combination (type 2), as well as thin layer joints taken from the particular masonry combination (type 3) is to be performed. The sample types are summarised in Figure 6.1. As the same masonry types are to be tested for the mechanical parameters (section 6.2), the samples must be taken from the same wall parts. Extra specimens of the type proposed for the validating creep and shrinkage experiments on wall parts in section 6.3 are proposed for this purpose.

The thin layer joints, a relatively modern trend in the building industry in The Netherlands, present a problem for sampling, being less than 3 mm thick. Therefore, a 2-constituent sample (type 3) is suggested for these combinations. As indicated, the type 1 specimens should be taken from the bricks/blocks in each orthogonal direction in order to capture orthotropy. Each entry in the last 3 columns of the table in Figure 6.1 represents a NMR test with upper air flow of relative humidity (RH) 50% at 20°C, Figure 6.2. The tests are to be repeated for absorption in a similar set-up, but with a constant moisture supply to one end, instead of the drying air flow in the desorption experiment shown.

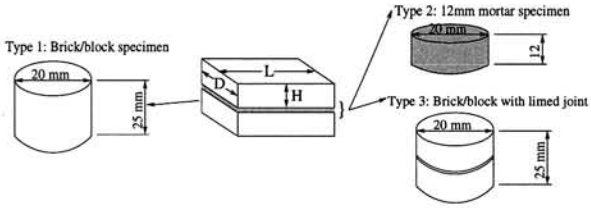

		Type and drilling direction Figure 6.1		
		L-dir	H-dir	D-dir
Specimen with 12 mm joint	Brick/block mortar	Type 1	Type 1 Type 2	Type 1
Specimen with thin layer joint	Combination		Type 3	

Figure 6.1: Specimen for NMR measurement

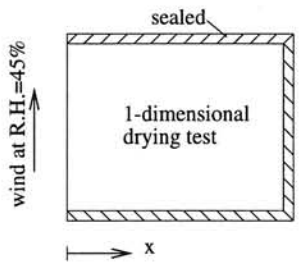

Figure 6.2: One-dimensional drying test for NMR measurement

To capture the statistical scatter for sampling, testing and material properties, at least three of each specimen should be prepared and tested.

6.1.2 Hygroscopic curves

Both sorption and desorption tests at 20°C are to be performed on each of the type 1 and 2 specimens in Figure 6.1 for at least nine nearly equally spaced humidity levels across the whole range of 0-100%, say with 10% intervals. To capture the statistical scatter for sampling, testing and material properties, at least three samples of each specimen should be prepared and tested.

6.1.3 Shrinkage coefficient

The volumetric change of the specimens used for determining the hygroscopic relations must be monitored. This enables the determination of the shrinkage coefficient as function of humidity $\alpha_s(h)$. Furthermore, as these specimens are reasonably thin, small hygral gradients and thus little or no cracking is expected, enabling the true material shrinkage coefficient to be determined. Having sampled the specimens from the three orthogonal directions in the units, information is available on the orthotropy of the material shrinkage.

By assuming the final shrinkage strains published by Van der Pluijm and Wubs (1996) for similar masonry, but for large wall parts ($\approx$ 450 mm x 450 mm x 10mm thick) shrinking at 20°C and RH 50% to be the material shrinkage at this climate, the axial shrinkage deformations for the types 1-3 specimens, Figure 6.1, can be estimated, Table 6.2. They serve as a guide for a choice of a suitable measuring device to ensure acceptable measuring accuracy. Note that the clay brick specimens of Van der Pluijm and Wubs (1996) were dry initially, causing subsequent swelling. No information thus exists from which to estimate the shrinkage in these specimens. Furthermore, the deformations will be fractions of those in the table, as the specimens will be subjected to small humidity changes at a time (10%, section 6.1.2), causing smaller volumetric changes per increment. The difference in the initial pore humidity and the environmental humidity in Van der Pluijm's experiments was up to RH 50%.

	ε_s^∞	ΔL_s (μm)		
	(Van der Pluijm 1996)	Type 1	Type 2	Type 3
1	-0.00035	8.8	4.2	
2	-0.00032			8.0
3	-0.00030	7.5	3.6	
4	-0.00030			7.5
7	-0.00020	5.0	2.4	
8	-0.00020			5.0

Table 6.2: Estimate of the gauge length final shrinkage deformation (ΔL_s).

6.2 Parameters of mechanical behaviour

As described in this report, section 5.3, and in the accompanying report Van Zijl (1999), many parameters are needed for the description of the mechanical response of masonry. However, much work has been done to characterise these parameters (Van der Pluijm and Vermeltfoort 1991, van der Pluijm 1992, Van Zijl 1996, Van Zijl et al. 1997). Tensile bond tests according to Van der Pluijm and Vermeltfoort (1991) must be performed on specimens of each masonry combination (Table 6.1). This parameter will suffice to estimate the remaining parameters with reasonable accuracy. In this section tests on small specimens are described for the determination of the parameters describing the time dependent mechanical behaviour of shrinkage and creep. The tests are designed to distinguish between the mechanisms captured by the numerical model described in this report. Drying creep, basic creep and free shrinkage are to be measured on separate specimens of the same type. In this manner the basic creep is established directly, allowing the stress-induced shrinkage to be derived accurately. The latter can only be achieved if cracking is avoided in the gauge area. This is possible by a careful choice of the shape, size and exposure of the specimens.

6.2.1 Specimen size and shape

Creep and shrinkage tests are to be performed on specimens with (type 1) and without a mortar joint (type 2) bored from masonry of each combination in Table 6.1 in accordance with Figure 6.3. By comparison of the responses of the two specimens of each type, parameters can be derived for describing the mortar behaviour.

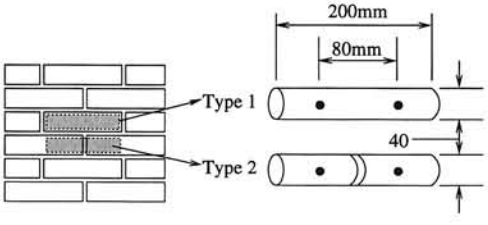

Figure 6.3: Masonry creep and shrinkage specimens.

6.2.2 Specimen types and fabrication

Specimens of each type in Figure 6.3 are to be bored from wall parts of each masonry type in Table 6.1. The same, or similar wall parts as those from which the specimens for measuring the moisture migration parameters are taken, section 6.1, should be used for this purpose. The proposed scheme of free shrinkage, basic and drying creep is shown in Figure 6.4. As indicated by hatching, only axial drying is allowed in the gauge area to avoid radial hygral and accompanying stress gradients, which may cause cracking. However, to compromise with limiting the time until hygral equilibrium is reached, a part of the specimens must be exposed that is as large as possible. Preliminary analyses indicate that the central 100 mm of each drying specimen should be sealed.

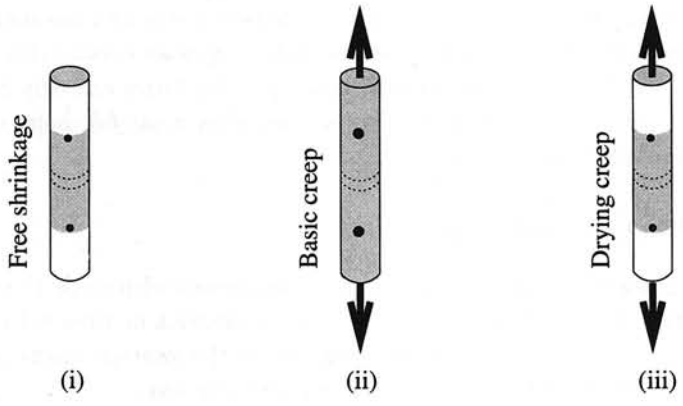

Specimen type	Specimen type number			
Figure 6.3	Free shrinkage	Basic creep	Drying creep	Strength test
Type 1	(i)	(ii)	(iii)	(iii)
Type 2	(i)	(ii)	(iii)	(iii)

Figure 6.4: Creep and shrinkage measurement scheme.

To capture the statistical scatter for sampling, testing and material properties, at least three samples of each specimen should be prepared and tested.

The constituent materials, preparation and fabrication procedures should be as described by Van der Pluijm and Wubs (1996).

6.2.3 Experimental set-up and procedure

At a curing age of 14 days, when the wall parts of section 6.3 are weighed and fitted with platens and gauge points, the moisture migration samples (section 6.1) and the just discussed creep and shrinkage samples should be taken from similar wall parts built specifically for the purpose.

Care has to be taken and an appropriate boring speed has to be selected to prevent damage to the joints. The specimens should be kept moist during the boring process and afterwards stored in an environment of 20°C and close to RH 100% (say RH 95%) until equilibrium is reached at this climate. The latter is ascertained by monitoring the weight until stabilisation. This procedure is required to

1) prevent cracking due to drying to a lower moisture content than at fabrication and
2) to ensure a known initial condition for the numerical simulation.

Once hygral equilibrium has been reached the gauge points and the connections for applying the creep load are to be glued into position with HBM X-60 (Van der Pluijm 1992). The gauge areas of the free drying and drying creep specimens must then be covered with a bituminous layer. Note that the free ends of the free drying specimens must also be sealed to ensure similar drying as in the case of the drying creep specimens. Subsequently all specimens must be wrapped in plastic and kept in the 20°C, RH 95% climate until their testing time.

The strength tests, column 5 in the table in Figure 6.4, should be performed first to determine the peak strength. Next, the creep specimens are to placed in the creep frames, taking care to only partially unwrap the plastic cover for handling and connection to avoid exposure. Once in place, the plastic cover is to be unwrapped before, with no time loss, application of the load. The creep load must be approximately one third of the peak strength, applied carefully, i.e. quasi-statically in several (say 5) equal steps, over a period of 5 minutes. The deformation must then be measured without delay to avoid bias of the initial, elastic deformation by significant creep deformation. To ensure similar procedures and human influence, one specimen should be set-up at a time in the sequence of 1) the sealed creep specimen, 2) the drying creep specimen and 3) the free shrinkage specimen. This sequence is to be kept for all subsequent measurements to ensure coinciding exposure times. Note that the creep load must be applied vertically to avoid bending effects.

6.2.4 Measurements

The measurements are to be taken between the gauge points indicated on Figure 6.3, both on the front and the back sides of each specimen. The deformations should be measured at specific times carefully chosen for proper characterisation also in the regions of great nonlinearity of the shrinkage/creep evolutions. A schedule of such times is proposed in

minutes			hours			days														
5	10	30	1	2	6	1	2	4	7	14	30	60	90	120	150	180	210	240	270	300

Table 6.3: Proposed time schedule for creep and shrinkage measurements.

Table 6.3. Small deformations, probably measured with no great accuracy, are expected at the early measurements, but should be performed, because they may provide valuable early age information at little extra cost. The first measurement is immediately after the total creep load has been applied, i.e. about 5 minutes after starting application of the load and drying. Note that also the free shrinkage specimen deformations measurement should be done according to this schedule. The slight discrepancy in creep time is acceptable. If the creep specimens are unwrapped only after load application, they may be damaged in the process.

The weight of the free shrinkage specimens must be measured at the same times for verification of the moisture migration analyses.

6.2.5 Estimates of load levels and deformations

A preliminary estimate of the peak loads and elastic, shrinkage and creep deformations is given in Table 6.4 for each specimen combination. With this knowledge and for a given requirement of measurement accuracy the measuring device can be chosen.

The deformations given in the table are based on one third of the lowest peak load of each masonry combination. This means that the same creep load must be applied to all specimens of the same combination, as the parameters for each constituent must be derived from the response of both types 1 and 2 specimens. The parameters used for the estimations are based on average values taken from Van der Pluijm and Vermeltfoort

	E_b	E_j	f_b	f_j	F_p (N)		ΔL_e (μm)		ΔL_{cr} (μm)		ΔL_s
	MPa	MPa	MPa	MPa	Type1	Type2	Type1	Type2	Type1	Type2	μm
1	11500	3300	2.0	0.1	2510	125	0.23	0.32	0.10	0.37	-28
2	11500		2.0		2510	2510	4.63	4.63	2.09	3.70	-28
3	11500	3300	2.0	0.1	2510	125	0.23	0.32	0.10	0.37	-24
4	11500		2.0		2510	2510	4.63	4.63	2.09	3.70	-24
5	16700	7700	2.0	0.6	2510	750	0.96	1.13		1.07	+8
6	16700		2.0		2510	2510	3.19	3.19		1.20	+8
7	17000	10350	2.0	0.7	2510	880	1.10	1.60		2.17	-16
8	17000		2.0		2510	2510	3.14	3.14		5.65	-16

Table 6.4: Estimate of peak tensile strength, total elastic (ΔL_e), shrinkage (ΔL_s) and creep (ΔL_{cr}) gauge length deformations in the different masonry combinations. E_b and E_j are the brick and mortar moduli of elasticity respectively, f_b and f_j the brick and interface tensile strengths.

(1991), Van der Pluijm (1992), Van der Pluijm and Wubs (1996). For type 1 specimens failure will occur in the brick, while failure in the brick/mortar interface is assumed for the type 2 specimens with the thick (12 mm) joints. The thin layer joints are mostly so strong that brick failure is expected in all the specimens of combinations 2, 4, 6 and 8.

The shrinkage and creep deformations are calculated from the shrinkage and compressive creep of the wall parts tested by Van der Pluijm (1996), built of the same combinations and exposed to the same climate as proposed for testing here. Note that these wall parts were built according to standard building procedure in The Netherlands. Therefore, the calcium silicate units were initially moisturised up to a level coinciding with RH $\approx$ 100% to ensure good bonding. This is also the initial condition proposed here, section 6.2.3. However, the clay bricks were dry at the time of manufacturing the walls, causing the swelling once they were exposed to the particular climate. Unfortunately, no data is available for estimating the shrinkage of these specimens when drying from RH 95% to RH 50%.

The creep deformation is based on creep experiments in compression, but scaled according to the lower (tensile) creep load. It can be seen that the creep is of an order lower than the shrinkage strain.

The increments in deformations between times of measurement according to Table 6.3 will be fractions of the total values, especially in the very early stages, calling for a measurement resolution of tens of nanometers.

6.2.6 Exposure to avoid cracking ánd excessive drying time

It has been stressed several times that cracking must be avoided within the gauge length to enable objective determination of the basic creep and the stress-induced shrinkage parameters. By numerical analyses of the moisture migration and the subsequent mechanical response of the specimens, Figure 6.3, the time until hygral equilibrium with the testing environment and thus the "final" shrinkage, can be estimated. For this purpose the combination 1 and 3, Table 6.1, specimens are analysed here, employing the hygral and mechanical parameters given in chapter 5.

For the mechanical analysis visco-elasticity is modelled, but no stress-induced shrinkage, which has been shown in section 5.9.3 to be conservative with regard to the stress levels. The constant shrinkage coefficients α_s estimated from experimental data, section 5.3, are employed, as are all the other moisture migration and mechanical model parameters described in chapter 5. Figure 6.5a shows the axi-symmetric model for numerical analysis schematically.

For the assumed slow diffusion of the combination 1 specimen, (KZB specimen, section 5.7.1), it is necessary to expose all but the gauge area to ensure a significant proportion of the final shrinkage ($\approx$ 75%) to occur within one year, Figure 6.5b, as opposed to only

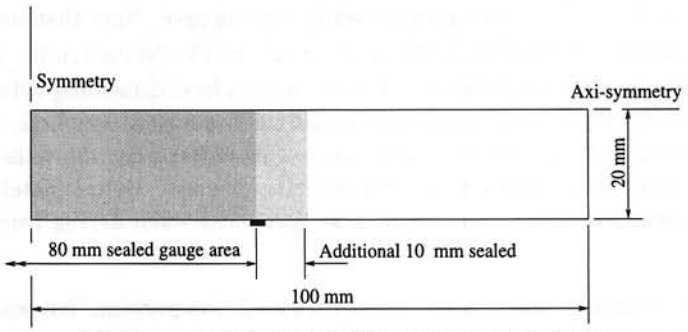

(a) Axi-symmetric model of free shrinkage specimen

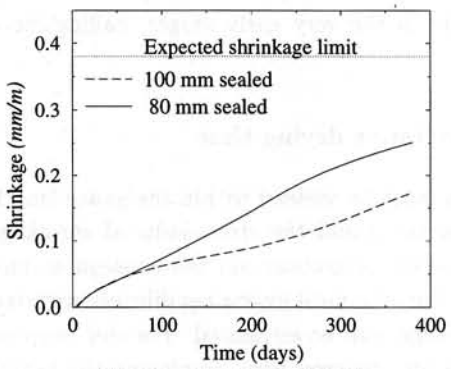

(b) Combination 1 (KZB)

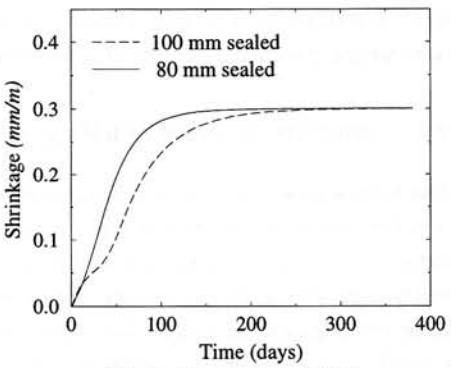

(c) Combination 3 (KZE)

Figure 6.5: Shrinkage evolution of combinations 1 and 3, Table 6.1, showing (a) the axi-symmetric model schematically, (b) combination 1 (KZB) and (c) 3 (KZE) shrinkage evolutions for two different levels of exposure.

50% if the central 100 mm, i.e. an additional 10 mm on each side of the gauge area, is sealed. For the higher diffusion rate of the KZE type specimens the final shrinkage is reached already after about 150 days, Figure 6.5c if the gauge area is sealed. It is recalled that the KZB diffusivity coefficient was taken as one tenth of the value derived from the NMR measured moisture profiles in drying sand-lime to obtain better agreement with the moisture loss evolution in KZB type wall parts of Van der Pluijm and Wubs (1996), section 5.7.1, 5.7.2. This was not necessary in the case of the KZE type wall parts, section 5.6. As discussed there, both the large elements in the KZE specimen and the WF bricks in the KZB specimens are of calcium silicate (sand-lime), but the different manufacturing processes cause them to have quite different properties. This is one of the main reasons for proposing the current experimental program. It is hoped that the WF units exhibit a higher diffusion rate than assumed here, enabling the total final shrinkage to be achieved within one year.

For both masonry types nearly axial moisture migration is found numerically in especially the lower part of the gauge area, as is confirmed by the low principal stresses in the KZB type 1 specimen with the central 100 mm sealed, Figure 6.6. An insignificant difference in the stress levels and patterns is found between the types 1 and 2 specimens. The price for the increased proportion of the final shrinkage achieved in one year by sealing only the gauge area, is the nonuniform drying, causing stress gradients with relatively high maximum values, Figure 6.7. The brick strength is not exceeded ($\sigma_1^{\max}$=1.2 MPa). However, by superimposing the average stress caused by the tensile creep load, which is one third of the bond strength, the bond strength is approached in the joint area. To be sure that no cracking will occur, the smaller exposure case should be opted for. In stead of extending the drying period, the one year data can be employed for deriving the model parameters. In this case a nonuniform axial shrinkage distribution will exist in the gauge area, as equilibrium will not have been reached. This will be have to be accounted for in deriving the parameters, but this presents no problem, as with knowledge of the true moisture migration and shrinkage coefficients from the first part of the proposed experiments, the shrinkage strain distribution can be found numerically.

For the KZE specimens sealing beyond the gauge area lowers the expected principal stresses, Figure 6.8, from the stresses when only the gauge area is sealed, Figure 6.9, but without the drawback of the long drying time. Equilibrium will have been reached within one year. As for the KZB specimens, insignificant difference in the stress levels and patterns is obtained between the type 1 and type 2 specimens.

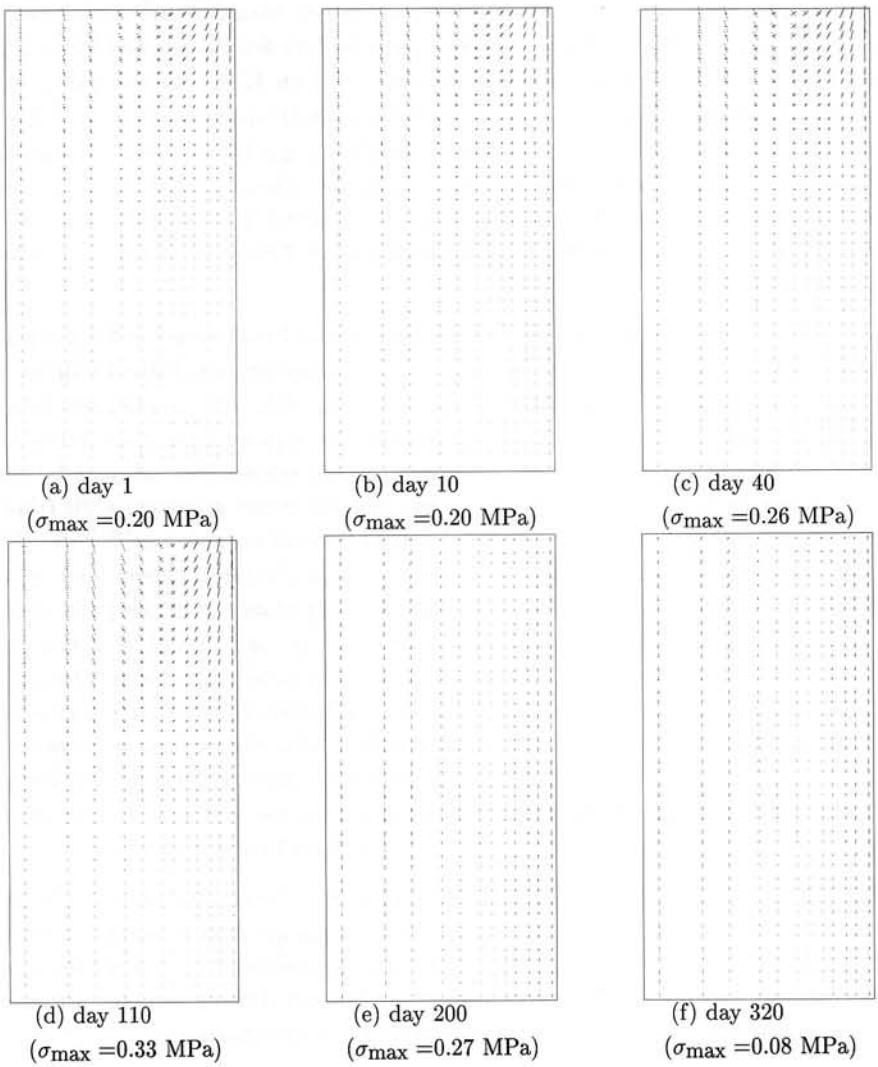

(a) day 1 (σ_{max} =0.20 MPa)

(b) day 10 (σ_{max} =0.20 MPa)

(c) day 40 (σ_{max} =0.26 MPa)

(d) day 110 (σ_{max} =0.33 MPa)

(e) day 200 (σ_{max} =0.27 MPa)

(f) day 320 (σ_{max} =0.08 MPa)

Figure 6.6: KZB type 1 specimen free shrinkage principal stresses. Central 100 mm sealed.

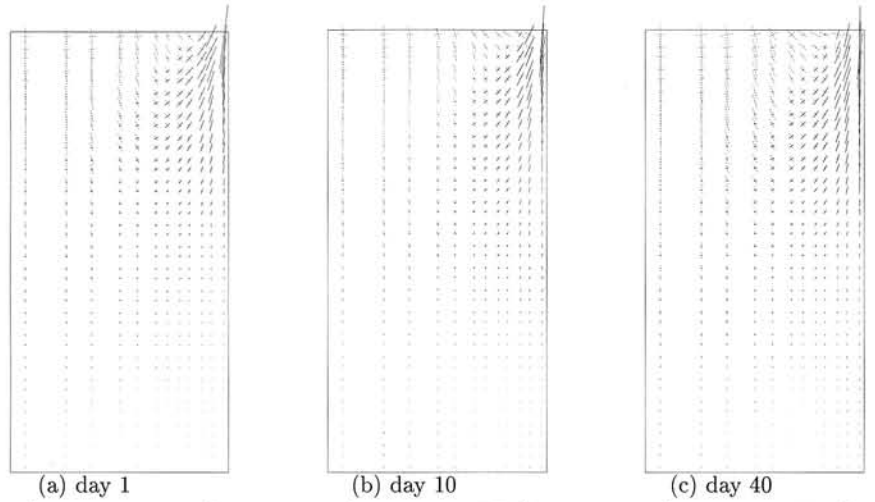

(a) day 1 (σ_{max} =1.17 MPa)

(b) day 10 (σ_{max} =1.09 MPa)

(c) day 40 (σ_{max} =1.10 MPa)

(d) day 110 (σ_{max} =0.46 MPa)

(e) day 200 (σ_{max} =0.15 MPa)

(f) day 320 (σ_{max} =0.05 MPa)

Figure 6.7: KZB type 1 specimen free shrinkage principal stresses. Only 80 mm gauge length sealed.

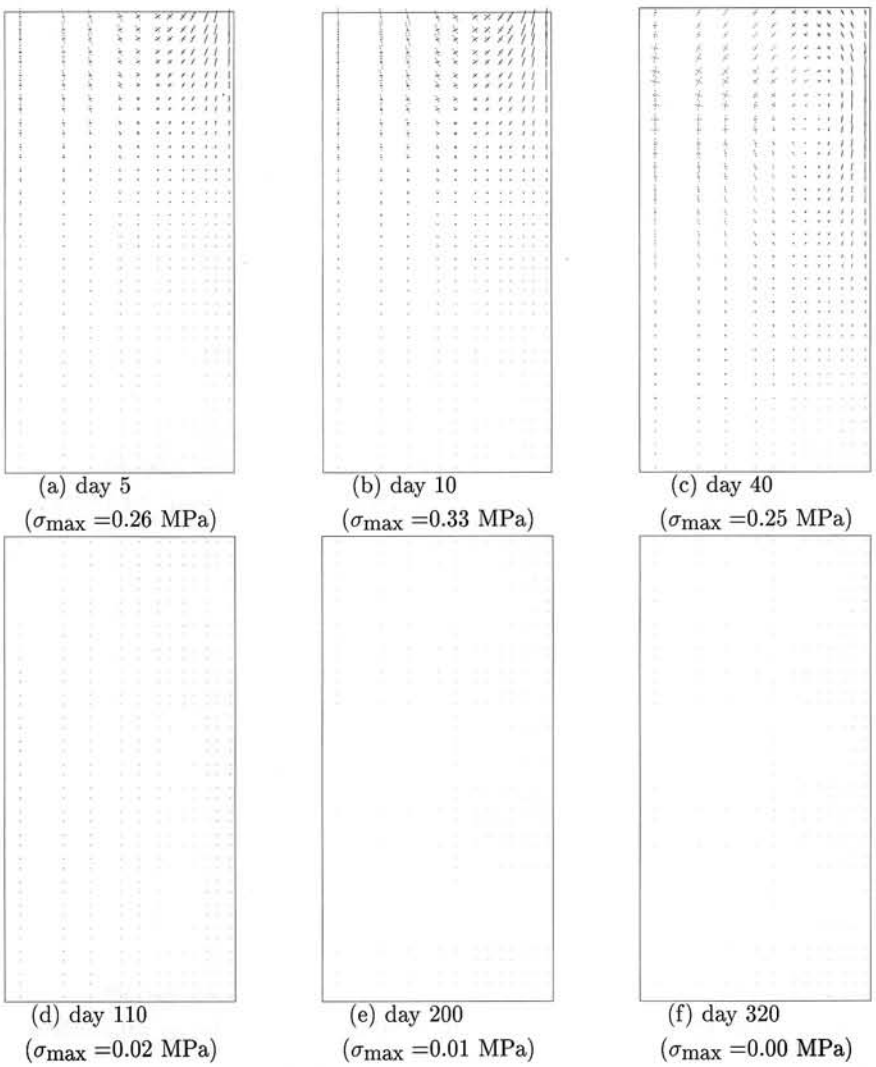

(a) day 5 (σ_{max} =0.26 MPa)
(b) day 10 (σ_{max} =0.33 MPa)
(c) day 40 (σ_{max} =0.25 MPa)
(d) day 110 (σ_{max} =0.02 MPa)
(e) day 200 (σ_{max} =0.01 MPa)
(f) day 320 (σ_{max} =0.00 MPa)

Figure 6.8: KZE type 1 free shrinkage specimen principal stresses. Central 100 mm sealed.

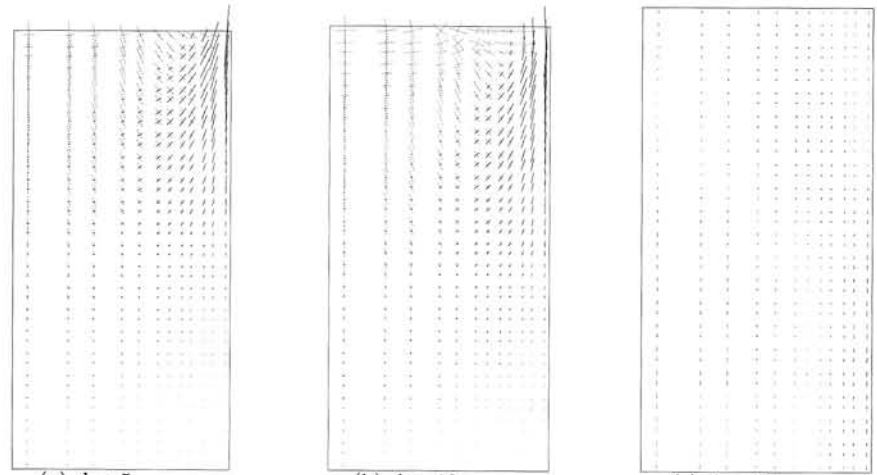

(a) day 5 (σ_{max} =1.17 MPa)

(b) day 10 (σ_{max} =0.96 MPa)

(c) day 40 (σ_{max} =0.09 MPa)

(d) day 110 (σ_{max} =0.01 MPa)

(e) day 200 (σ_{max} =0.00 MPa)

(f) day 320 (σ_{max} =0.00 MPa)

Figure 6.9: KZE type 2 free shrinkage specimen principal stresses. Only 80 mm gauge length sealed.

6.3 Validation experiments on wall parts

For the verification of the model parameters derived from the above described experiments, as well as for the validation of the modelling strategy, wall parts, Figure 6.10, are to be fabricated and tested for creep and shrinkage. Furthermore, the results of such measurements provide data for the homogenisation of the two-phase material for more elegant and computationally viable continuum analysis of large masonry structures. Once again, tensile creep is of importance, being a major factor in damage caused by restrained shrinkage of masonry walls.

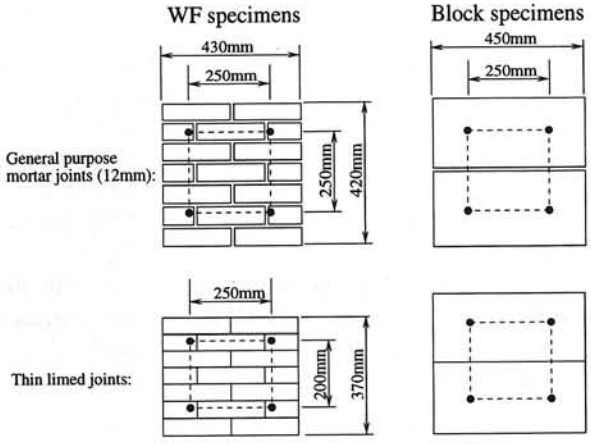

Figure 6.10: WF and large block specimens for creep and shrinkage measurements.

6.3.1 Specimen size and shape

The specimen size, Figure 6.10, is a compromise between a sample that is large enough, including several head (vertical) and bed (horizontal) joints in the gauge length to represent in-plane masonry wall behaviour, and that is small enough to restrict experimental cost. Due to the relatively low tensile strength, restricting the creep load to one third of the peak load, the creep deformations are of an order lower than the shrinkage, requiring a gauge length of sufficient size to be able to accurately measure the deformations. This requirement is in conflict with the specimen size restriction, forcing measurement to areas influenced by boundary conditions. The boundaries of the steel loading plate glued to the specimens have thus to be simulated to a sufficient degree of accuracy in the numerical analyses.

The units in the block specimens have to be sawn to the indicated dimensions, Figure 6.10, from large elements. However, the dimensions indicated in Figure 6.10 for the WF specimens are average values. The particular dimensions are determined by the prescribed

	Calcium silicate	Fired-clay	Concrete
Length *(mm)*	214	205	210
Height *(mm)*	53	47	50
Thickness *(mm)*	102	96	100

Table 6.5: Brick sizes for determination of wall part dimensions.

12 and 3 mm joints respectively, and the brick sizes as delivered by the manufacturers. An indication of the brick sizes is given in Table 6.5.

6.3.2 Specimen types and fabrication

All the masonry combinations and specimens to be prepared and tested are tabulated in Figure 6.11. All the masonry types given in Table 6.1 are repeated for clarity, while also the proposed loading orientations are distinguished.

Note that, apart from the global strength tests in column 8 and 9 of the table, only the shrinkage and creep parameters are determined. The other mechanical parameters, such as bond strength, frictional and dilatancy angle and fracture energies (section 5.3) of the masonry combinations of interest have been characterised during the last decade (Van der Pluijm and Vermeltfoort 1991, Van der Pluijm 1992, Van Zijl 1996, Van Zijl et al. 1997). Additional tensile bond strength tests on two units joined with a single joint (Van der Pluijm 1992), of mortar or glue, depending on the combination of interest, will suffice to characterise the other parameters to an acceptable degree of accuracy. If budget requirements are strict, the bond strength can be estimated from the wall part peak strength obtained from the strength tests in column 8 and 9 of Figure 6.11.

To capture the statistical scatter for sampling, testing and material properties, at least three samples of each specimen should be prepared and tested.

The constituent materials, preparation and fabrication procedures should be as described by Van der Pluijm and Wubs (1996). As mentioned before, extra wall parts of each type should be built for sampling the moisture migration specimens, section 6.1, and the small creep and shrinkage specimens of section 6.2.

6.3.3 Experimental set-up and procedure

After fabrication all specimens should be wrapped up in plastic (Van der Pluijm and Wubs 1996) to avoid loss of moisture. After 14 days of curing weight measurement of all specimens should be done. Directly thereafter, the load platens and gauge points must be glued into position with HBM X-60 (Van der Pluijm 1992). It will be necessary to vary the glue layer thickness to ensure proper, rectangular positioning of the platens. A maximum thickness of 3 mm may not be exceeded, however. The basic creep specimens must then be sealed with a bituminous layer. Because the specimens must be unpacked from the

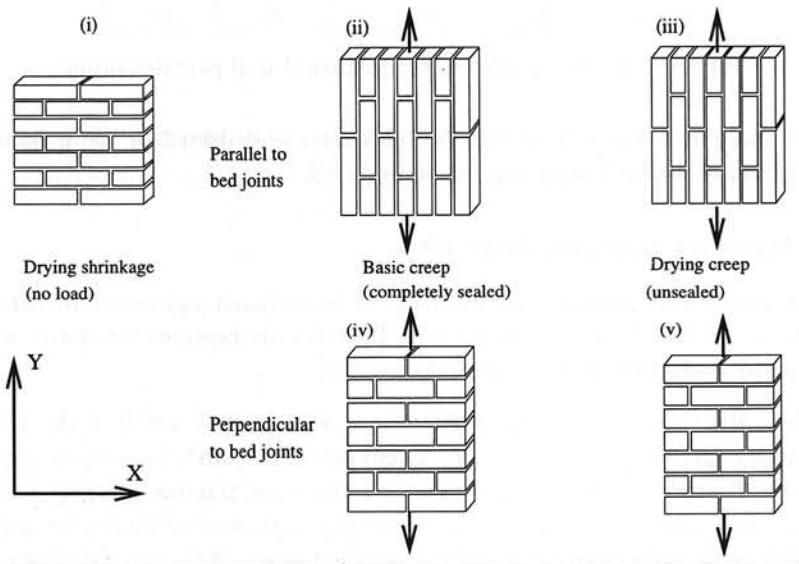

	Specimen	Specimen type number - Figure 6.11						
		"Free" shrink	Basic creep X	Dry creep X	Basic creep Y	Dry creep Y	Strength test X	Strength test Y
1	Calcium silicate brick with 12 mm joint	(i)	(ii)	(iii)	(iv)	(v)	(iii)	(v)
2	Calcium silicate brick with thin layer joint	(i)	(ii)	(iii)	(iv)	(v)	(iii)	(v)
3	Calcium silicate block with 12 mm joint	(i)	(ii)	(iii)	(iv)	(v)	(iii)	(v)
4	Calcium silicate block with thin layer joint	(i)	(ii)	(iii)	(iv)	(v)	(iii)	(v)
5	Fired-clay brick with 12 mm joint	(i)	(ii)	(iii)	(iv)	(v)	(iii)	(v)
6	Fired-clay brick with thin layer joint	(i)	(ii)	(iii)	(iv)	(v)	(iii)	(v)
7	Concrete brick with 12 mm joint	(i)	(ii)	(iii)	(iv)	(v)	(iii)	(v)
8	Concrete brick with thin layer joint	(i)	(ii)	(iii)	(iv)	(v)	(iii)	(v)

Figure 6.11: Masonry wall part creep and shrinkage measurement scheme.

plastic for weighing, gluing and sealing, one should be handled at a time to minimise the exposure time until re-wrapping. If possible, the specimens should be stored or at least handled (weighed and glued) in a climate of RH 95% to minimise moisture loss. A further 14 days of curing should be allowed for development of the maximum bond strength, before commencing with the tests.

For all the tests constant humidity (50%) and temperature (20°C) should be maintained. As mentioned before, the *Pickett*-effect is to be isolated by testing three specimens of each type, i.e. a free drying, drying creep and a sealed/basic creep specimen. These samples are shown schematically for WF brick specimen in Figure 6.11(i)-(iii). To also investigate orthotropy, two more, similar specimens (iv & v, Figure 6.11) should be prepared and tested as by tensile loading perpendicular to bed joints. Note that the creep loads must be applied vertically to avoid the frictional resistance on the lower platen if tested horizontally.

The strength tests, column 8 and 9 in Figure 6.11, should be performed first to find the peak strength. Next the creep specimens are to placed in the creep frames, plastic cover for handling and connection. Once in place, the plastic cover is to be unwrapped before, with no time loss, application of the load. The creep load must be approximately one third of the peak strength, applied carefully, i.e. quasi-statically in several (5) equal steps, over a period of 5 minutes. The deformation must then be measured without delay to avoid bias of the initial, elastic deformation by significant creep deformation. To ensure a similar procedure and human influence, one specimen should be set-up at a time in the sequence of 1) the sealed creep specimen, 2) the drying creep specimen and 3) the free shrinkage specimen. This sequence is to be kept for all subsequent measurements to ensure coinciding exposure times.

6.3.4 Measurements

The measurements have to be taken between the gauge points indicated on Figure 6.10, both on the front and back sides of each specimen. The deformations should be measured at specific times carefully chosen for proper characterisation also in the regions of great nonlinearity of the shrinkage/creep evolutions. A schedule of such times is proposed in Table 6.6. Small deformations, probably measured with no great accuracy are expected at the early measurements, but should be performed, because they may provide valuable early age information at little extra cost. The first measurement is immediately after the total creep load has been applied, i.e. about 5 minutes after starting application of the load and drying. Note that also the free shrinkage specimen deformations measurement should be done according to this schedule. The slight discrepancy in creep time is acceptable. If the creep specimens are unwrapped only after (tensile) load application, they may be damaged in the process.

minutes			hours			days													
5	10	30	1	2	6	1	2	4	7	14	30	60	90	120	150	180	210	240	270	300

Table 6.6: Proposed time schedule for creep and shrinkage measurements.

Apart from the deformations, the weight of the free shrinkage specimens must be measured at these times for verification of the moisture migration analyses.

6.3.5 Estimates of load levels and deformations

A preliminary estimate of the peak loads and elastic, shrinkage and creep deformations is given here for each specimen combination. With this knowledge and for a given requirement of measurement accuracy the measuring device can be chosen. The peak strength is taken as the minimum of the resisting forces which cause the assumed failure modes shown in Figure 6.12. For a creep load of one third of the peak strength, the total elastic and creep deformation of the gauge length is estimated by a simple elastic calculation, ignoring, for instance, the staggered bond. These estimates are summarised in Table 6.7.

It is emphasized that the parameters used in Table 6.7 are based on average values taken from Van der Pluijm and Vermeltfoort (1991), Van der Pluijm (1992), Van der Pluijm and Wubs (1996), as well as educated guesses. The shrinkage deformations are calculated from the shrinkage of wall parts (Van der Pluijm and Wubs 1996) of the same combinations and exposed to the same climate as proposed for testing here. Note that these wall parts were built according to standard building procedure in The Netherlands. Therefore, the calcium silicate units are initially moisturised up to a level coinciding with RH $\approx$ 100%. This causes the significant shrinkage in these specimens. However, the clay bricks are dry

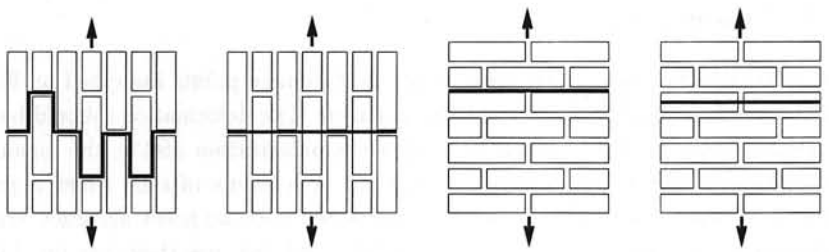

$$F_p \approx min\left[\ \left(f_j L_{f_j} + c_j L_{c_j}\right),\ \left(f_j L_{f_j} + f_b L_{f_b}\right),\ \left(f_j L_{f_j}\right),\ \left(f_j L_{f_j} + f_b L_{f_b}\right)\ \right] t$$

where
f_j = joint tensile strength, L_{f_j} = total length of joint failing in tension
f_b = brick tensile strength, L_{f_b} = total length of brick failing in tension
c_j = joint cohesion, L_{c_j} = total length of joint failing in shear
t = wall part thickness.

Figure 6.12: Assumed wall part failure modes.

at the time of manufacturing the walls, causing the swelling once they are exposed to the particular climate.

The creep deformation is based on creep experiments in compression, but scaled according to the lower (tensile) creep load, assuming proportionality and equal behaviour for compressive and tensile creep. It can be seen that the creep is one to two orders lower than the shrinkage strain, with the smallest values for loading perpendicular to the bed joints (configuration (v), Figure 6.11). The increments in deformations between times of measurement according to Table 6.6 will be fractions of the total values, especially in the very early stages, calling for a measurement resolution in the order of one hundred nanometers.

	Type fig. 6.11	f_b MPa	f_j MPa	c_j MPa	F_p N	E_b MPa	E_j MPa	ΔL_e μm	ΔL_{cr} μm	ΔL_s μm
1	(iii)	2.0	0.1	0.3	22580	11500	3300	4.3	4.8	-87.5
	(v)				4320			1.1	1.2	-92.5
2	(iii)	2.0			73600	11500		14.5	11.6	-80.0
	(v)				84600			11.6	9.3	-72.0
3	(iii)	2.0	0.1	0.3	82120	11500	3300	14.5	16.0	-62.5
	(v)				4500			0.8	0.9	-75.0
4	(iii)	2.0			84400	11500		14.8	11.8	-62.5
	(v)				90000			14.5	11.6	-75.0
5	(iii)	2.0	0.6	0.9	46320	16700	7700	5.8	5.5	+25.0
	(v)				25920			3.7	3.5	-25.0
6	(iii)	2.0			73600	16700		10.0	5.0	+25.0
	(v)				84600			8.0	4.0	-20.0
7	(iii)	2.0	0.7	1.2	49040	17000	10350	5.9	10.6	-50.0
	(v)				30240			3.9	6.9	-75.0
8	(iii)	2.0			73600	17000		9.8	17.6	-50.0
	(v)				84600			7.8	14.2	-60.0

Table 6.7: Estimate of peak tensile strength, total elastic (ΔL_e), shrinkage (ΔL_s) and creep (ΔL_{cr}) gauge length deformations in the different masonry combinations for both loading directions.

Chapter 7

CONCLUSION

A numerical model for the analysis of moisture migration in cementitious material has been elaborated. The link with volume change and the subsequent mechanical response of such materials has been established in a simplified way. Some dangers and difficulties of the nonlinear diffusion analysis required in the modelling approach have been highlighted and illustrated. The application of the approach to a two-phase material, such as masonry, has been discussed and illustrated. The limited experimental data in the literature has been exploited for the characterisation of the material parameters needed for describing masonry creep and shrinkage. However, the experiments were not devised to distinguish between the mechanisms acting, such as the basic creep, cracking and stress-induced shrinkage. This calls for iterative adjustment of the parameters and reanalysis until convergence to a set of parameters with which the measured behaviour can be simulated numerically with acceptable accuracy. The first iteration of this process was performed and reported. A total lack of some of the parameters, for instance the stress-induced shrinkage coefficients, renders this inverse engineering procedure impossible. Moreover, the modelling approach and the parameters obtained in the above way can only be claimed valid if different sets of experimental results can be reproduced with them. Therefore, no further iterations were done, opting rather for an experimental program. The proposed program is specifically designed to distinguish between mechanisms in order to facilitate parameter derivation. For validation, experiments on masonry wall parts will be performed simultaneously.

Appendix A

TWO-PHASE DIFFUSION: PERFECT HYDRAULIC INTERFACE

The assumption of hydraulically perfect brick/mortar interfaces implies that (eg. Pel 1995)

$$h_b = h_m. \tag{A.1}$$

For the general case that the hygroscopic relations for brick and mortar differ, a discontinuity in moisture content occurs at the interface:

$$\theta_b\left(h_b\right) \neq \theta_m\left(h_m\right) \tag{A.2}$$

To illustrate this discontinuity in moisture content at the interface, the single jointed KZE specimen described in chapter 5 is investigated. Figure A.1 shows the pore humidity and moisture content profiles along a vertical line in the centre of the specimen. The pore humidities are solved from eq. (2.9) directly without any constraints at the interfaces. Subsequently the respective hygroscopic relations (Figure 5.2) are employed to translate the pore humidities to moisture contents. These profiles are in qualitative agreement with moisture content profiles measured in small masonry specimens (Brocken and Pel 1997).

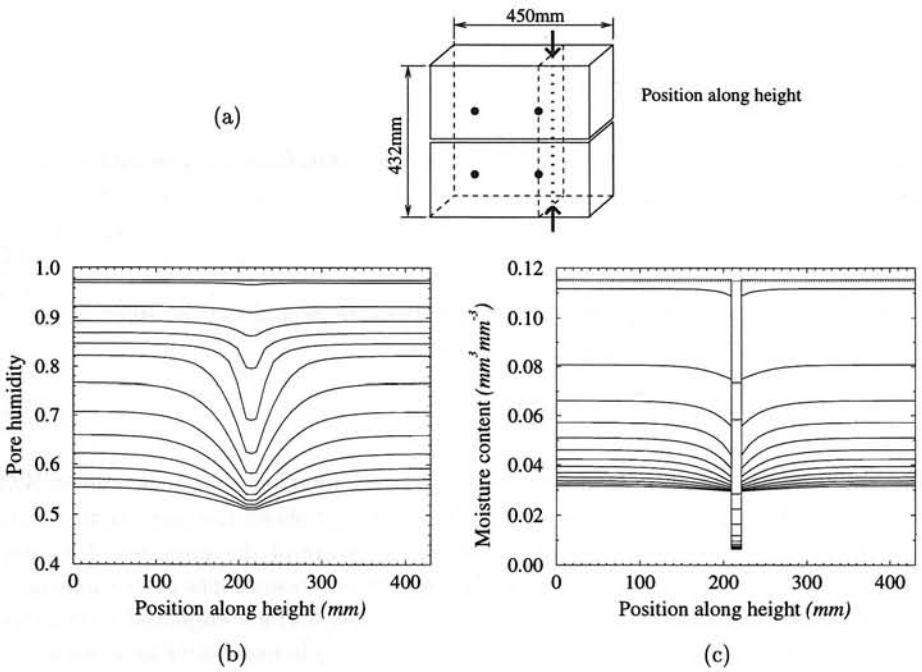

Figure A.1: Illustration of the moisture content discontinuity across the mortar interface. (a) Line along which the evolution of the (b) pore humidity and (c) moisture content is shown in the single-jointed, drying calcium silicate masonry specimen (KZE). The profiles are shown for 1 hour, 1 day and subsequently with 10 day intervals.

Appendix B

COEFFICIENT SMOOTHNESS: TIME AND SPATIAL DISCRETISATION CONSTRAINT

As can be seen in the numerical simulation of the 1-dimensional drying experiments of Pel (1995), Figure 4.4, there are some differences between the solution of eq. (2.5) for moisture content and eq. (2.9) for pore humidity, with subsequent translation to moisture content via the hygroscopic relation $(\theta - h)$. This is due to the additional restriction in terms of spatial discretisation if the equations are "non-smooth", i.e. continuous and therefore differentiable in the domain of interest, but with large gradients in some localised areas. See for instance the calcium silicate hygroscopic relation in Figure 4.1.

To further illustrate this point, a "smooth" case is analysed here. Consider a one-dimensional 100 mm long bar of a cementitious material drying axially from an initial moisture content of 0.1 (mm^3/mm^3) in an environment of relative humidity of 40% $(h_E = 0.4)$. The smooth diffusivity and hygroscopic relations are shown in Figure B.1. An eight-element uniform discretisation for FE solution gives nearly exact agreement between the numerical results from both differential equations, Figure B.2.

Now consider that the same bar, discretised with eight elements, is made of calcium silicate with the moisture migration parameters shown before for the KZE specimen, Figure 5.2. For the hygroscopic curve $\theta(h)_a$ fitted to the data points shown in Figure B.3a, a large discrepancy is found when comparing the solutions of the two differential equations, Figure B.3b. Employing the smoother curve $\theta(h)_b$ produces a large improvement.

Yet, a discrepancy between the solutions persists. If the discretisation is refined to 100 elements, good agreement is obtained, Figure B.4.

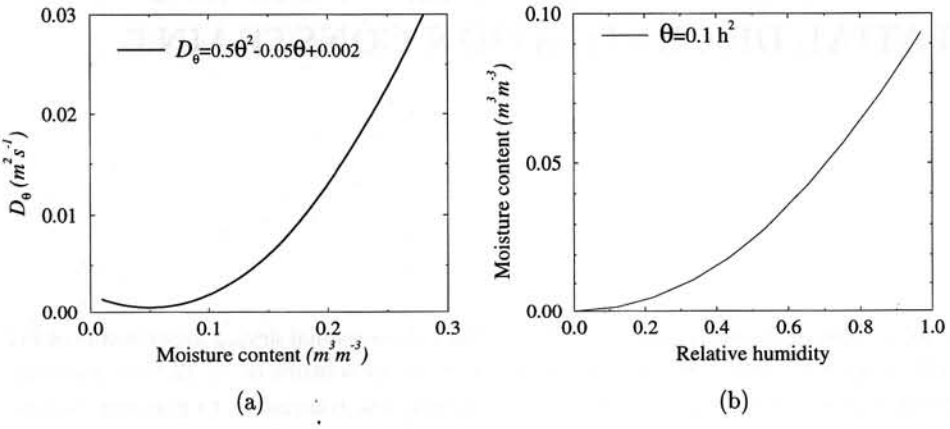

Figure B.1: "Smooth" (a) diffusivity and (b) hygroscopic relation for one-dimensional drying example.

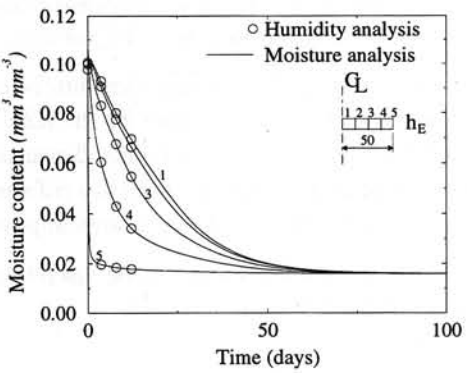

Figure B.2: Moisture profiles in axially drying bar with smooth parameters obtained from moisture content and pore humidity equations respectively.

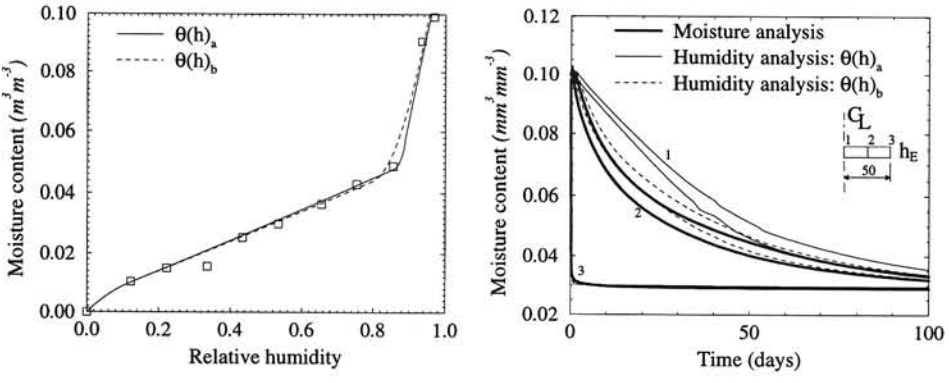

Figure B.3: (a) Smooth and non-smooth curves fitted to experimentally measured hygroscopic data. (b) Moisture profiles obtained from moisture content and pore humidity analyses, employing both hygroscopic curves shown in (a).

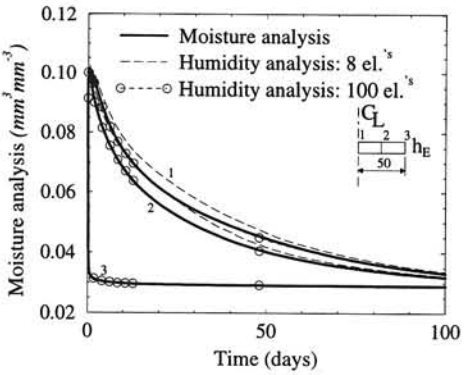

Figure B.4: Moisture profiles obtained from moisture content and pore humidity equations respectively in axially drying bar with smooth parameters.

Appendix C

PLANE (2D) ANALYSIS VS. 3D ANALYSIS

To investigate whether a two-dimensional (plane) analysis suffices to capture the drying behaviour, discrete analyses of moisture migration have been performed, employing the two-dimensional and three-dimensional meshes of the KZE specimen, chapter 5, shown in Figure C.1. Note that symmetry is assumed, requiring only one eighth of the specimen to be modelled. The material parameters of section 5.2 and the boundary conditions of section 5.5 apply.

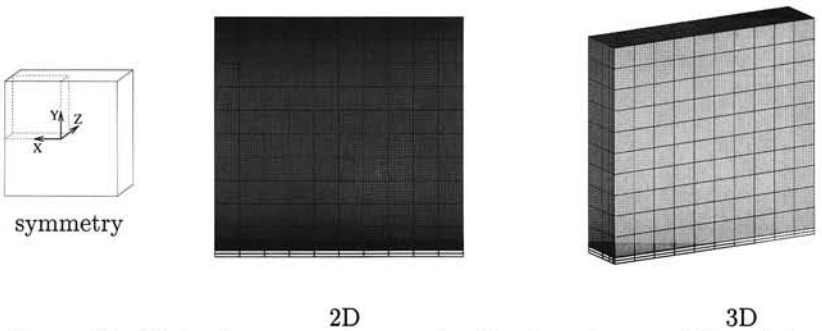

Figure C.1: Finite element meshes employed to investigate validity of plane analysis.

Converting the computed pore humidities to moisture content via the hygroscopic relations $(\theta - h)$, subsequent integration over the total volume and multiplication with the liquid water mass density, the total moisture content by mass is found. The moisture content evolution is compared in Figure C.2a. Clearly the plane analysis greatly overestimates the drying rate. By increasing the diffusion coefficient in the thickness direction ten times, the two-dimensional drying rate is approached, as also shown in Figure C.2a. Thus, despite the fact that the thickness of a masonry wall is small compared with its plane dimensions, the low diffusivity requires discretisation also in the thickness direction, thus a three-dimensional analysis, if the true humidity and shrinkage gradients and accompanied eigenstressing are to be considered. The pore humidity gradient through the thickness

is illustrated by Figure C.2b, where humidity evolution at the nodal points through the thickness are shown.

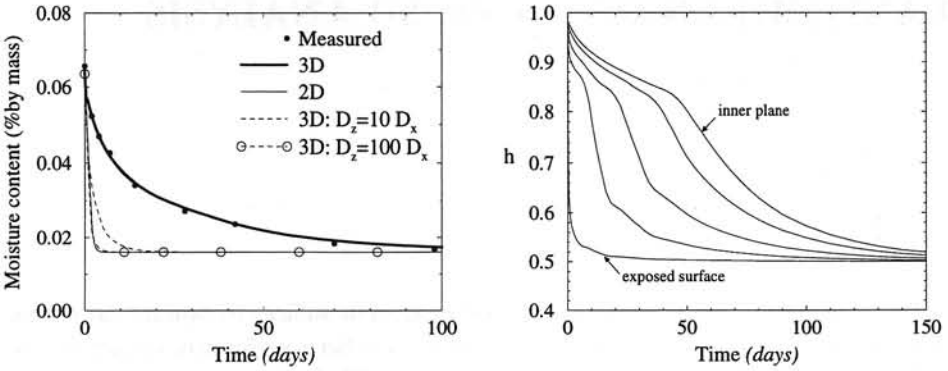

Figure C.2: (a) Comparison of moisture content evolutions obtained by 3D and 2D analyses. (b) Pore humidity gradient through thickness.

Appendix D

OVERSHOOT: TIME AND SPATIAL DISCRETISATION CONSTRAINT

Selection of time and spatial discretisation is a crucial issue for accurate numerical analysis of moisture transport and accompanied shrinkage. This issue has been discussed in section 5.4, but is further illustrated here at the hand of the analyses of the drying KZE specimen. Specifically, the influence of the film coefficient as retarder of the moisture migration, is investigated. The extreme case of immediate surface hygral equilibrium, as is the case when an infinitely large surface convection/film coefficient is employed, is analysed and compared with the case of finite surface convection ($\beta = 5mm/day$).

In Figure D.1 the numerically obtained pore humidity and moisture content profiles are compared for the two cases of surface boundary conditions. It is clear that the increased drying rate when employing the infinite film coefficient, Figure D.1c-d, causes *overshoot* for this particular choice of mesh refinement. The β =5 mm/day convection coefficient sufficiently retards the surface drying rate to avoid *overshoot.*

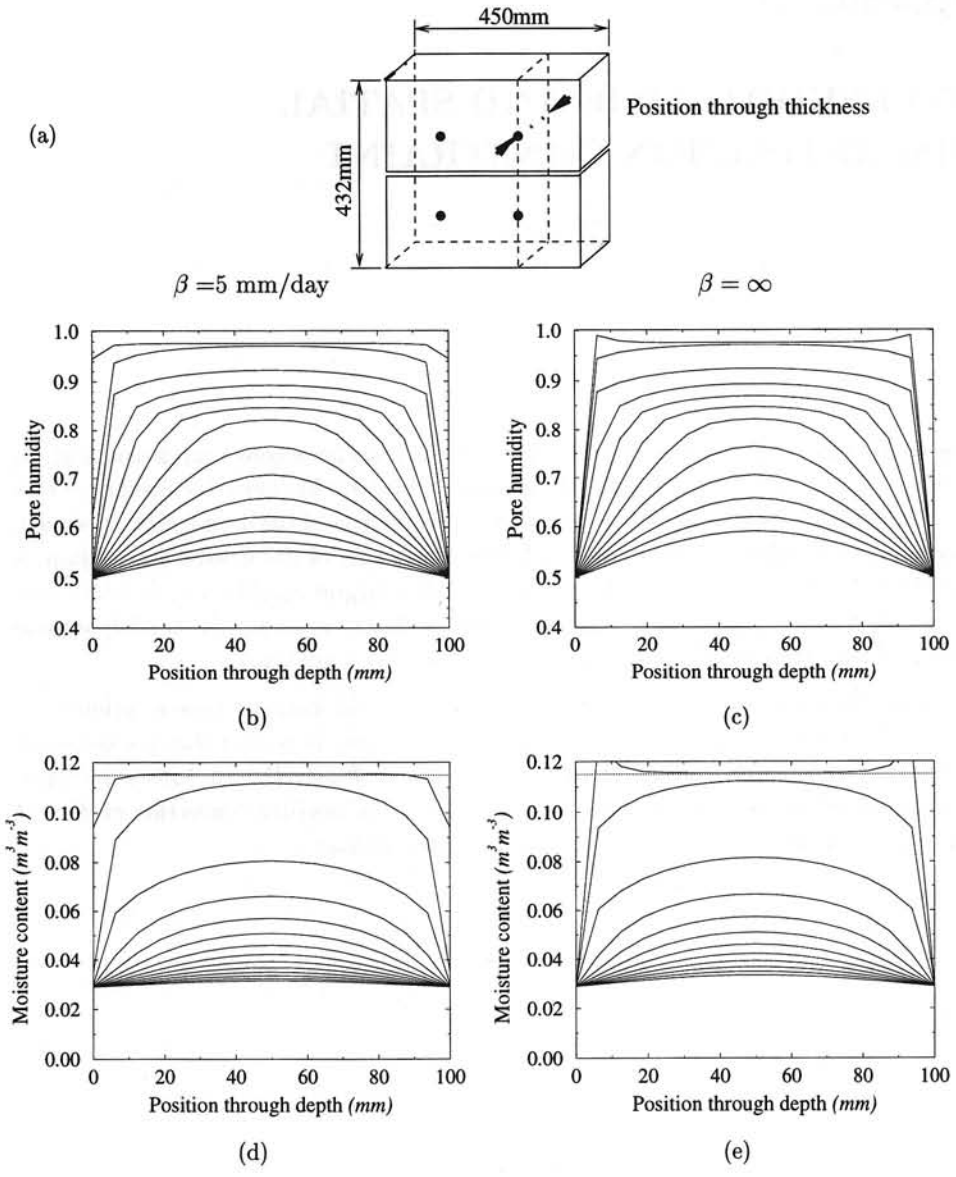

Figure D.1: Illustration of the overshoot if rapid surface convection is modelled. (a) Line along which evolution of pore humidity profiles are shown for (b) β =5 mm/day film coefficient and (c) immediate surface equilibrium with environment ($\beta = \infty$). The overshoot is even more pronounced for moisture content: (d) and (e). The profiles shown occur in the single-jointed, drying calcium silicate masonry specimen (KZE) and are shown for 1 hour, 1 day and subsequently 10 day intervals.

REFERENCES

Alvaredo, A.M. (1994) **Drying shrinkage and crack formation**. Building materials reports No 5, ETH Laboratory for building materials, Zürich, Switzerland.

Alvaredo, A.M., Hebling, A. and Wittmann, F.H. (1995) **Shrinkage data of drying concrete**, Building materials reports No 4, ETH Laboratory for building materials, Zürich, Switzerland.

Bažant, Z.P., Ed. (1988) **Mathematical Modeling of Creep and Shrinkage of Concrete**. John Wiley and Sons.

Bažant, Z.P. and Najjar, L.J. (1971) Drying of concrete as a nonlinear diffusion problem. **Cement and Concrete Research**, 1(5), 461-473.

Bažant, Z.P. and Xi, Y. (1993) New test method to separate microcracking from drying creep: Curvature creep at equal bending moments and various axial forces, in **Creep and Shrinkage of Concrete** (eds. Z.P. Bažant and I. Carol), E.&F.N.Spon, London, 77-82.

Bažant, Z.P., Sener, S. and Kim, J-K. (1987) Effect of Cracking on Drying Permeability and Diffusivity of concrete. **ACI Materials Journal**, 351-357.

Bear, J. and Bachmat, Y. (1990) **Introduction to modeling of transport phenomena in porous media**. Volume 4, Kluwer, Dordrecht, The Netherlands.

Brocken, H.J.P. and Pel, L. (1997) Moisture transport over the brick-mortar interface: water absorption and drying, in **Int. Brick/Block Masonry Conf.** (eds. Mingshun Wu, Yiliang Qian, Xiaozu Su and Xianglin Gu), Shanghai, 826-835.

Brocken, H.J.P., Pel, L., Smolders, H.R. and Kopinga, K. (1997) Moisture transport in brick masonry: water absorption. Submitted to **Bldg. and Envir.**

Brunauer, S., Emmet, P.H. and Teller, E. (1938) Adsorption of gases in multimolecular layers. **J. of Amer. Chem. Soc.**, 60, 309-319.

Brunauer, S., Skalny, J. and Boder, E.E. (1939) Adsorption on nonporous solids. **J. of Colloid and Interface Science**, 30(4), 546-552.

L'Hermite, R. and Mamillan, M. (1968) Retrait et fluage des bétons (in French). **Annales ATBTP**, 21(249), 1319-1337.

Lourenço, P.B. (1996) **Computational strategies for masonry structures**. Dissertation, Delft Univ. of Techn., Delft, The Netherlands.

Pel, L. (1995) **Moisture transport in porous building materials**. Dissertation, Eindhoven Univ. of Techn., Eindhoven, The Netherlands.

Philip, J.R. and De Vries, D.A. (1957) Moisture movement in porous materials under temperature gradients, **Trans. Am. Geophys. Un.**, 38(2), 222-232.

Shrive, N.G., Sayed-Ahmed, E.Y. and Tilleman, D. (1997) . Creep analysis of clay masonry assemblages, **Canadian J. of Civil Eng.**, 24(3):367-379.

Tammes, E. and Vos, B.H. (1984) **Heat and moisture transport in building structures** (in Dutch). Kluwer, Deventer-Antwerpen.

Tanabe, T. and Ishikawa, Y. (1993) Time-dependent behaviour of concrete at early ages and its modeling, in **Creep and Shrinkage of Concrete** (eds. Z.P. Bažant and I. Carol), E.&F.N.Spon, London, 435-452.

Van der Pluijm, R. (1992) **Deformation controlled shear tests on masonry**. Report BI-92-104, TNO-Bouw, Delft, The Netherlands.

Van der Pluijm, R. and Vermeltfoort, A.T. (1991) **Deformation controlled tension and compression tests on units, mortar and masonry**. Report B-91-0561, TNO-Bouw, Delft, The Netherlands.

Van der Pluijm, R. and Wubs, A.J. (1996) **The time dependent deformational behaviour of masonry** (in Dutch). Report 96-CON-R0901-02, TNO Building and Construction, Delft, The Netherlands. TNO Building and Construction, Delft, The Netherlands.

Van Zijl, G.P.A.G. (1996) **Masonry micro-shear behaviour along bed joints**. Report 03-21-22-0-01, Delft Univ. of Techn., Delft, The Netherlands.

Van Zijl, G.P.A.G. (1999) **A numerical formulation for masonry creep, shrinkage and cracking**. Report LR-TM-99-03, Delft Univ. of Techn., Delft, The Netherlands.

Van Zijl, G.P.A.G., De Borst, R. and Rots, J.G. (1998) FE analysis of the interaction between moisture migration, creep, shrinkage and cracking, in **Computational modelling of concrete structures** (eds. H. Mang, N. Bićanić and R. de Borst), Balkema, Amsterdam, 505-511.

Van Zijl, G.P.A.G., Lourenço, P.B. and Rots, J.G. (1997) Non-associated plasticity formulation for masonry interface behaviour, in **Computational Plasticity: Fundamentals and Applications** (eds. D.R.J. Owen, E. Oñate and E. Hinton), Barcelona, 1586-1593.

Whitaker, S. (1977) Simultaneous heat, mass and momentum transfer in porous media. **Adv. Heat Transfer**, 13, 119-200.

Xi, Y., Bažant, Z.P. and Molina, L. (1993) Improved pore water diffusion model for creep analysis of concrete structures, in **Creep and Shrinkage of Concrete** (eds. Z.P. Bažant and I. Carol), E.&F.N.Spon, London, 169-174.

LIST OF FIGURES

4.1 Isothermal sorption curves (Pel 1995) for masonry constituents. 11

4.2 (a) 1-Dimensional drying test for measuring (b) moisture profiles (Pel 1995), using NMR. 12

4.3 Diffusivity variation with moisture content for various building materials (Pel 1995). 14

4.4 Moisture profiles obtained by FE solution of the nonlinear diffusion equation (a) for moisture content θ and (b) pore humidity h, moisture content subsequently being calculated from the hygroscopic relation $\theta(h)$. 14

5.1 (a) Masonry shrinkage specimens investigated. (b) One eighth of each specimen modelled by assumption of symmetry. 16

5.2 (a) Diffusion coefficient variation with moisture content and (b) isothermal desorption curves (Pel 1995). 18

5.3 (a) Measured creep and fitted five-element Dirichlet function. (b) Relaxation function derived from (a). 20

5.4 Humidity evolution at points through the masonry specimen thickness for (a) uniform and (b) nonuniform spatial discretisation in the thickness direction. 23

5.5 (a-d) Pore humidity contours and (e) moisture content (% by mass) evolution in drying single joint calcium silicate (KZE) specimen. 25

5.6 (a-d) Contours of maximum principal stress and (e) total strain in the gauge length in *free* drying single joint calcium silicate (KZE) specimen. . . 26

5.7 KZE *drying* and *basic* creep response. 27

5.8 Assumed (a) desorption curve and (b) diffusion coefficient for the calcium silicate WF specimen. 28

5.9 (a-d) Pore humidity contours and (e) moisture content (% by mass) evolution in drying WF calcium silicate (KZB) specimen. 30

5.10 (a-d) Contours of maximum principal stress and (e) total strain in the gauge length in *free* drying WF calcium silicate (KZB) specimen. 31

5.11 (a-d) Contours of maximum principal stress in KZB drying creep specimen. (e) Total strain (y direction) in the gauge length in KZB creep specimen subjected to shrinkage (*drying creep*) and with free shrinkage subtracted (*basic creep*). 32

5.12 Finite element meshes employed to investigate mesh objectivity of the numerical simulation of the KZB shrinkage specimen. 33

5.13 (a) Moisture content (by mass) and (b) total strain in the gauge length for the three meshes employed, Figure 5.12. 34

5.14 Influence of surface convection coefficient on masonry moisture content. . . 35

5.15 Influence of shrinkage coefficient dependence on humidity on *free* shrinkage. 36

5.16 (a) "Free" shrinkage evolution and (b) stress distribution through the thickness at the gauge point in the KZE specimen. 37

5.17 Illustration of Pickett-effect in (a) KZE and (b) KZB creep specimen. . . . 38

5.18 Influence of bulk creep on (a) KZE and (b) KZB masonry *free* shrinkage. . 39

5.19 Determination of *basic* creep for (a) KZE and (b) KZB masonry. 40

6.1 Specimen for NMR measurement 45

6.2 One-dimensional drying test for NMR measurement 45

6.3 Masonry creep and shrinkage specimens. 47

6.4 Creep and shrinkage measurement scheme. 48

6.5 Shrinkage evolution of combinations 1 and 3, Table 6.1, showing (a) the axi-symmetric model schematically, (b) combination 1 (KZB) and (c) 3 (KZE) shrinkage evolutions for two different levels of exposure. 52

6.6 KZB type 1 specimen free shrinkage principal stresses. Central 100 mm sealed. 54

6.7 KZB type 1 specimen free shrinkage principal stresses. Only 80 mm gauge length sealed. 55

6.8 KZE type 1 free shrinkage specimen principal stresses. Central 100 mm sealed. 56

6.9 KZE type 2 free shrinkage specimen principal stresses. Only 80 mm gauge length sealed. 57

6.10 WF and large block specimens for creep and shrinkage measurements. . . . 58

6.11 Masonry wall part creep and shrinkage measurement scheme. 60

6.12 Assumed wall part failure modes. 62

A.1 Illustration of the moisture content discontinuity across the mortar interface. (a) Line along which the evolution of the (b) pore humidity and (c) moisture content is shown in the single-jointed, drying calcium silicate masonry specimen (KZE). The profiles are shown for 1 hour, 1 day and subsequently with 10 day intervals. 68

B.1 "Smooth" (a) diffusivity and (b) hygroscopic relation for one-dimensional drying example. 70

B.2 Moisture profiles in axially drying bar with smooth parameters obtained from moisture content and pore humidity equations respectively. 70

B.3 (a) Smooth and non-smooth curves fitted to experimentally measured hygroscopic data. (b) Moisture profiles obtained from moisture content and pore humidity analyses, employing both hygroscopic curves shown in (a). . 71

B.4 Moisture profiles obtained from moisture content and pore humidity equations respectively in axially drying bar with smooth parameters. 71

C.1 Finite element meshes employed to investigate validity of plane analysis. . 73

C.2 (a) Comparison of moisture content evolutions obtained by 3D and 2D analyses. (b) Pore humidity gradient through thickness. 74

D.1 Illustration of the overshoot if rapid surface convection is modelled. (a) Line along which evolution of pore humidity profiles are shown for (b) β =5 mm/day film coefficient and (c) immediate surface equilibrium with environment ($\beta = \infty$). The overshoot is even more pronounced for moisture content: (d) and (e). The profiles shown occur in the single-jointed, drying calcium silicate masonry specimen (KZE) and are shown for 1 hour, 1 day and subsequently 10 day intervals. 76

LIST OF TABLES

5.1 Mechanical material parameters employed for calcium silicate brick and element specimens. 19

5.2 Dilatancy parameters employed. 19

5.3 Shrinkage coefficients derived from final shrinkage strain values of masonry shrinkage specimens. 22

5.4 Shrinkage coefficients derived from final shrinkage values of cement pastes at different environmental humidities (Alvaredo et al 1995). 36

6.1 Typical Dutch masonry types to be tested. 43

6.2 Estimate of the gauge length final shrinkage deformation (ΔL_s). 46

6.3 Proposed time schedule for creep and shrinkage measurements. 50

6.4 Estimate of peak tensile strength, total elastic (ΔL_e), shrinkage (ΔL_s) and creep (ΔL_{cr}) gauge length deformations in the different masonry combinations. E_b and E_j are the brick and mortar moduli of elasticity respectively, f_b and f_j the brick and interface tensile strengths. 50

6.5 Brick sizes for determination of wall part dimensions. 59

6.6 Proposed time schedule for creep and shrinkage measurements. 62

6.7 Estimate of peak tensile strength, total elastic (ΔL_e), shrinkage (ΔL_s) and creep (ΔL_{cr}) gauge length deformations in the different masonry combinations for both loading directions. 63

Series 01: Aerodynamics

01. F. Motallebi, 'Prediction of Mean Flow Data for Adiabatic 2-D Compressible Turbulent Boundary Layers'
1997 / VI + 90 pages / ISBN 90-407-1564-5
02. P.E. Skåre, 'Flow Measurements for an Afterbody in a Vertical Wind Tunnel'
1997 / XIV + 98 pages / ISBN 90-407-1565-3
03. B.W. van Oudheusden, 'Investigation of Large-Amplitude 1-DOF Rotational Galloping'
1998 / IV + 100 pages / ISBN 90-407-1566-1
04. E.M. Houtman / W.J. Bannink / B.H. Timmerman, 'Experimental and Computational Study of a Blunt Cylinder-Flare Model in High Supersonic Flow'
1998 / VIII + 40 pages / ISBN 90-407-1567-X
05. G.J.D. Zondervan, 'A Review of Propeller Modelling Techniques Based on Euler Methods'
1998 / IV + 84 pages / ISBN 90-407-1568-8
06. M.J. Tummers / D.M. Passchier, 'Spectral Analysis of Individual Realization LDA Data'
1998 / VIII + 36 pages / ISBN 90-407-1569-6
07. P.J.J. Moeleker, 'Linear Temporal Stability Analysis'
1998 / VI + 74 pages / ISBN 90-407-1570-X
08. B.W. van Oudheusden, 'Galloping Behaviour of an Aeroelastic Oscillator with Two Degrees of Freedom'
1998 / IV + 128 pages / ISBN 90-407-1571-8
09. R. Mayer, 'Orientation on Quantitative IR-thermografy in Wall-shear Stress Measurements'
1998 / XII + 108 pages / ISBN 90-407-1572-6
10. K.J.A. Westin / R.A.W.M. Henkes, 'Prediction of Bypass Transition with Differential Reynolds Stress Models'
1998 / VI + 78 pages / ISBN 90-407-1573-4
11. J.L.M. Nijholt, 'Design of a Michelson Interferometer for Quantitative Refraction Index Profile Measurements'
1998 / 60 pages / ISBN 90-407-1574-2
12. R.A.W.M. Henkes / J.L. van Ingen, 'Overview of Stability and Transition in External Aerodynamics'
1998 / IV + 48 pages / ISBN 90-407-1575-0
13. R.A.W.M. Henkes, 'Overview of Turbulence Models for External Aerodynamics'
1998 / IV + 40 pages / ISBN 90-407-1576-9
14. G. Schouten, 'The Two-Dimensional Soundfield of a Vortex Moving Around the Sharp Edge of a Half-Plane'
1998 / VI + 26 pages / ISBN 90-407-1730-3
15. M.M.J. Schoones / W.J. Bannink, 'Base Flow and Exhaust Plume Interaction. Part 1: Experimental Study'
1998 / VIII + 64 pages / ISBN 90-407-1747-8

16. M.M.J. Schoones / E.M. Houtman, 'Base Flow and Exhaust Plume Interaction. Part 2: Computational Study'
1998 / VIII + 86 pages / ISBN 90-407-1748-6

Series 02: Flight Mechanics

01. E. Obert, 'A Method for the Determination of the Effect of Propeller Slipstream on a Static Longitudinal Stability and Control of Multi-engined Aircraft'
1997 / IV + 276 pages / ISBN 90-407-1577-7
02. C. Bill / F. van Dalen / A. Rothwell, 'Aircraft Design and Analysis System (ADAS)'
1997 / X + 222 pages / ISBN 90-407-1578-5
03. E. Torenbeek, 'Optimum Cruise Performance of Subsonic Transport Aircraft'
1998 / X + 66 pages / ISBN 90-407-1579-3

Series 03: Control and Simulation

01. J.C. Gibson, 'The Definition, Understanding and Design of Aircraft Handling Qualities'
1997 / X + 162 pages / ISBN 90-407-1580-7
02. E.A. Lomonova, 'A System Look at Electromechanical Actuation for Primary Flight Control'
1997 / XIV + 110 pages / ISBN 90-407-1581-5
03. C.A.A.M. van der Linden, 'DASMAT-Delft University Aircraft Simulation Model and Analysis Tool. A Matlab/Simulink Environment for Flight Dynamics and Control Analysis'
1998 / XII + 220 pages / ISBN 90-407-1582-3
04. S.K. Advani, 'The Kinematic Design of Flight Simulator Motion-Bases'
1998 / XVIII + 244 pages / ISBN 90-407-1671-4
05. J.M. Maciejowski, 'Predictive Control. A Lecture Course Given in the Aerospace Engineering Faculty TU Delft'
1998 / XII + 156 pages / ISBN 90-407-1714-1
06. J.C. Gibson, 'Development of a methodology for excellence in handling qualities design for fly by wire aircraft'
1999 / XII + 240 pages / ISBN 90-407-1842-3

Series 05: Aerospace Structures and Computional Mechanics

01. A.J. van Eekelen, 'Review and Selection of Methods for Structural Reliability Analysis'
1997 / XIV + 50 pages / ISBN 90-407-1583-1
02. M.E. Heerschap, 'User's Manual for the Computer Program Cufus. Quick Design Procedure for a CUt-out in a FUSelage version 1.0'
1997 / VIII + 144 pages / ISBN 90-407-1584-X
03. C. Wohlever, 'A Preliminary Evaluation of the B2000 Nonlinear Shell Element Q8N.SM'
1998 / IV + 44 pages / ISBN 90-407-1585-8
04. L. Gunawan, 'Imperfections Measurements of a Perfect Shell with Specially Designed Equipment (UNIVIMP)
1998 / VIII + 52 pages / ISBN 90-407-1586-6

Series 07: Aerospace Materials

01. A. Vašek / J. Schijve, 'Residual Strenght of Cracked 7075 T6 Al-alloy Sheets under High Loading Rates'
1997 / VI + 70 pages / ISBN 90-407-1587-4
02. I. Kunes, 'FEM Modelling of Elastoplastic Stress and Strain Field in Centre-cracked Plate'
1997 / IV + 32 pages / ISBN 90-407-1588-2
03. K. Verolme, 'The Initial Buckling Behavior of Flat and Curved Fiber Metal Laminate Panels'
1998 / VIII + 60 pages / ISBN 90-407-1589-0
04. P.W.C. Provó Kluit, 'A New Method of Impregnating PEI Sheets for the *In-Situ* Foaming of Sandwiches'
1998 / IV + 28 pages / ISBN 90-407-1590-4
05. A. Vlot / T. Soerjanto / I. Yeri / J.A. Schelling, 'Residual Thermal Stresses around Bonded Fibre Metal Laminate Repair Patches on an Aircraft Fuselage'
1998 / IV + 24 pages / ISBN 90-407-1591-2
06. A. Vlot, 'High Strain Rate Tests on Fibre Metal Laminates'
1998 / IV + 44 pages / ISBN 90-407-1592-0
07. S. Fawaz, 'Application of the Virtual Crack Closure Technique to Calculate Stress Intensity Factors for Through Cracks with an Oblique Elliptical Crack Front'
1998 / VIII + 56 pages / ISBN 90-407-1593-9
08. J. Schijve, 'Fatigue Specimens for Sheet and Plate Material'
1998 / VI + 18 pages / ISBN 90-407-1594-7
09. J. Schijve, 'The Significance of Fractography for Investigations of Fatigue Crack Growth under Variable-Amplitude Loading'
1998 / IV + 34 pages / ISBN 90-407-1716-8

10. M.J.L. van Tooren / Z.C. Roza, 'Finite Difference Methods for Stress Analysis of Adhesive Bonded Joints. The Design of a MATLAB Adhesive Toolbox'
1998 / VIII + 94 pages / ISBN 90-407-1717-6
11. A. Vlot / S. Verhoeven / P.J.M. Nijssen 'Bonded Repairs for Aircraft Fuselages'
1998 / VIII + 82 pages / ISBN 90-407-1804-0

Series 08: Astrodynamics and Satellite Systems

01. E. Mooij, 'The Motion of a Vehicle in a Planetary Atmosphere'
1997 / XVI + 156 pages / ISBN 90-407-1595-5
02. G.A. Bartels, 'GPS-Antenna Phase Center Measurements Performed in an Anechoic Chamber'
1997 / X + 70 pages / ISBN 90-407-1596-3
03. E. Mooij, 'Linear Quadratic Regulator Design for an Unpowered, Winged Re-entry Vehicle'
1998 / X + 154 pages / ISBN 90-407-1597-1

Series 11: Engineering Mechanisms

01. G.P.A.G. van Zijl, 'A Numerical Formulation for Masonry Creep, Shrinkage and Cracking'
1999 / VIII + 88 pages / ISBN 90-407-1892-X
02. G.P.A.G. van Zijl, 'A Numerical Formulation for Moisture Migration in Masonry'
1999 / VIII + 86 pages / ISBN 90-407-1893-8

3029083

The moisture content and migration in cementitious materials determine its time dependent response. Much research has been done over the last decades to gain insight in these phenomena and to distinguish between true and apparent mechanisms of creep and shrinkage. However, experimentally as well as computationally much remains to be done to characterise the indentified role players, for instance, true material shrinkage, stress-induced shrinkage, basic creep and the coupled effect of cracking and accelerated moisture migration. This contribution addresses these issues. A numerical model for the finite element analysis of creep, shrinkage and cracking in cementitious materials has been described in an accompanying report (Van Zijl 1999). Here, a model is elaborated for analysing the moisture migration, the underlying mechanism of shrinkage and creep. The coupling with the mechanical analysis is also described.

The material of interest is masonry, to be regarded as a particular cementitious concretelike material. Existing experimental data on masonry is employed for the model parameter estimation and the validation. However, the experiments were not devised to distinguish between the different phenomena included in the numerical model. This excludes the possibility of the estimation of parameters even by an inverse approach. For this reason an experimental program is proposed with specific tests on small specimens for determining the model parameters and separate tests of wall parts on the meso-scale for the validation of the model.

ISBN 90-407-1893-8

DELFT AEROSPACE
ENGINEERING & TECHNOLOGY